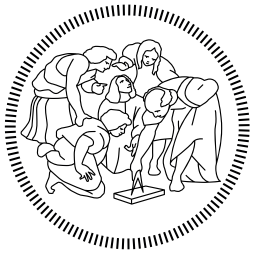

POLITECNICO
MILANO 1863

Performance of a VFP Engine: Thermal Evaluation of a Water-cooled Nozzle and Ballistic Analysis

Tesi di Laurea Magistrale in
Aeronautical and Space Engineering - Ingegneria Aeronautica e Spaziale

Davide Fellegara, 10498072
Luca Pecchini, 10671536

Abstract: A Hybrid Rocket Engine (HRE) is a thermo-chemical propulsion system that stores fuel and oxidizer in two different states of aggregation. HREs feature multiple advantages such as operating flexibility compared to Solid Rocket Motors, lower architectural complexity with respect to traditional Liquid Rocket Engines and reduced costs both due to the architecture and fuel price. However, traditional fuel formulations employed in HREs exhibit low regression rates and the propellants require prolonged mixing for an efficient combustion. This results in HREs having usually a high length-to-diameter ratio (L/D) or more complex grain geometries to increase thrust, leading to structural challenges and reduced volumetric efficiencies. Additionally, the diffusive flame in HREs leads to combustion efficiencies relatively lower than the other thermo-chemical propulsion systems. These limitations have hindered the application of hybrid rockets in both launch and in-space scenarios. The Vortex Flow Pancake (VFP) system represents an unconventional configuration for a HRE. In this design, a tangential oxidizer injection generates a vortex flow field in the combustion chamber, which is delimited by the space within the two solid fuel discs. The space between the two discs is smaller than their diameter, resulting in a compact engine characterized by a $L/D < 1$. The swirling flow results in improved mixing of the propellants, therefore enhancing the combustion efficiency. On top of that, the tangential oxidizer flux provides thermal protection to the combustion chamber side walls against the flame. Furthermore, this innovative design drastically reduces the O/F shift phenomenon during combustion, which is a commonly observed drawback in traditional HREs. This research aims at modeling a heat transfer problem to evaluate the power subtracted from the expanding exhaust gas of the VFP engine, developed at Politecnico di Milano (SVFP), by its water-cooled nozzle. The first part of this work consists in the formulation of a thermal model capable of describing the problem through the use of empirical correlations taken from literature. Once the problem is described, a code is then used to analyze temperature data from multiple experimental tests. Finally, a CFD analysis is employed to calibrate this code and make it more accurate. The results demonstrated the functionality of the code by providing an estimate of the temperatures reached by the nozzle and the thermal power extracted by the cooling chamber from the exhaust gases in a variety of firing conditions. Furthermore, a comprehensive ballistic analysis was conducted using data from the tests for various fuel formulations.

Advisor:
Prof. Christian Paravan

Co-advisors:
Eng. Valerio Santolini

Academic year:
2022-2023

Key-words: Hybrid Rocket Engine, Thermo-chemical propulsion, Vortex Flow Pancake, Heat transfer problem, Water-cooled nozzle, Thermal model, Ballistic analysis, Computational Fluid Dynamics (CFD)

Nomenclature

-	Description
ABS	Acrylonitrile Butadiene Styrene
AP	Ammonium perchlorate
BL	Boundary layer
CB	Carbon powder
CEA	Chemical equilibrium with applications
CFD	Computational fluid dynamics
FDM	Fused deposition modeling
FIR	Finite impulse response
fu	Fuel
GOX	Gaseous oxygen
HRE	Hybrid rocket engine
HTC	Heat transfer coefficient
$HTPB$	Hydroxyl-terminated polybutadiene
LRE	Liquid tocket engine
L/D	Length over diameter ratio
NO	Top fuel disk
$N2$	Bottom fuel disk
O/F	Oxidizer to fuel ratio
ox	Oxidizer
$PETG$	Polyethylene terephthalate glycol
$SEBS-MA$	Styrene Ethylene Butylene Styrene - Maleic Anhydride
$SVFP$	SPLab Vortex flow pancake
TOT	Thickness over time
VDC	Volts of direct current
VFP	Vortex flow pancake

List of Symbols

Variable	Description	Unit
$\boldsymbol{\alpha}$	Fraction of nozzle	$-$
$\boldsymbol{\beta}$	Thermal expansion coefficient	$-$
$\boldsymbol{\Delta t_b}$	Burning time	s
$\boldsymbol{\Delta T_w}$	Water temperature increment	K
$\boldsymbol{\Delta m^i_{grain}}$	Mass burned of a generic grain "i"	g
$\boldsymbol{\Delta m_{tot}}$	Total mass burned	g
$\boldsymbol{\Delta t_{static}}$	Time window where the weight of the apparatus on the load-cell is offset	s
$\boldsymbol{\epsilon}$	Expansion ratio	$-$
$\boldsymbol{\eta_{c^*}}$	Characteristic velocity efficiency	$-$
$\boldsymbol{\lambda}$	Correction factor for the global convective heat transfer coefficient	$-$
$\boldsymbol{\mu_w}$	Water dynamic viscosity	Ns/m^2
$\boldsymbol{\nu_w}$	Water kinematic viscosity	m^2/s
$\boldsymbol{\rho_w}$	Water density	Kg/m^3
$\boldsymbol{\rho}$	Density	Kg/m^3
$\boldsymbol{\sigma}$	Standard deviation	$-$
$\boldsymbol{\phi}$	Diameter	mm
$\boldsymbol{A_e}$	Nozzle exit area	mm^2
$\boldsymbol{A_f}$	Burning surface	mm^2
$\boldsymbol{A_n}$	Nozzle surface area	mm^2
$\boldsymbol{A_t}$	Nozzle throat area	mm^2
$\boldsymbol{a_r}$	Proportional coefficient	$-$
$\boldsymbol{Bi}$	Biot number	$-$
$\boldsymbol{c^*}$	Characteristic velocity	m/s
$\boldsymbol{c^*_{CEA}}$	Nasa CEA characteristic velocity	m/s
$\boldsymbol{c^*_{real}}$	Experimental characteristic velocity	m/s
$\boldsymbol{c_{p,n}}$	Nozzle specific heat	J/kgK
$\boldsymbol{c_{p,w}}$	Specific heat of water	J/kgK
$\boldsymbol{D}$	Characteristic length of the nozzle	mm
$\boldsymbol{D_f}$	Fuel grain external diameter	mm
$\boldsymbol{D_i}$	Fuel grain central perforation diameter	mm
$\boldsymbol{G_{tot}}$	Total mass flux	kg/m^2s
$\boldsymbol{g}$	Gravity acceleration	m/s^2
$\boldsymbol{h}$	Convective heat transfer coefficient	W/m^2K
$\boldsymbol{h_{cc}}$	Combustion chamber height	mm
$\boldsymbol{h_{cc,0}}$	Combustion chamber initial height	mm
$\boldsymbol{h_{cc,f}}$	Combustion chamber final height	mm
$\boldsymbol{h_{forced}}$	Forced convection convective heat transfer coefficient	W/m^2K
$\boldsymbol{h_{free}}$	Free convection convective heat transfer coefficient	W/m^2K
$\boldsymbol{h_{wn}}$	Water-nozzle global convective heat transfer coefficient	W/m^2K
$\boldsymbol{k_c}$	Copper thermal conductivity	W/mK
$\boldsymbol{k_w}$	Water thermal conductivity	W/mK

Variable	Description	Unit
$\dot{m}$	Mass flow rate	g/s
$\dot{m}_t$	Total mass flow rate	g/s
$\dot{m}_{ox}$	Oxidizer mass flow rate	g/s
$\dot{m}_f$	Fuel mass flow rate	g/s
$\dot{m}_{CT}$	Carbon tube mass flow rate	g/s
Nu	Nusselt number	$-$
n_r	Exponential coefficient	$-$
Pr	Prandtl number	$-$
p	Pressure	MPa
p_{cc}	Combustion chamber pressure	MPa
p_{cl}	Classical pressure with centrifugal component	MPa
p_v	Pressure at the center of the vortex	MPa
$\dot{Q}$	Heat power	W
$\dot{Q}_{gas}$	Heat power subtracted from the gas	W
$\dot{Q}_n$	Nozzle heat power	W
$\dot{Q}_{wv}$	Water volume heat power	W
R^2	Coefficient of determination	$-$
Ra	Rayleigh number	$-$
R_{cond}	Equivalent conductive heat transfer resistance	K/W
R_{conv}	Equivalent convective heat transfer resistance	K/W
Re	Reynolds number	$-$
r_f	Regression rate	mm/s
$r_{f,avg}$	Average regression rate	mm/s
$r^i_{f,avg}$	Average regression rate of a generic grain "i"	mm/s
T	Thrust	N
T_{avg}	Average thrust	N
T_{film}	Film temperature in walls proximity	K
$T_{measured}$	Measured thrust	N
T_n	Nozzle temperature	K
T_{static}	Static thrust	N
T_w	Water temperature	K
$T_{w,in}$	Water temperature at the inlet of the cooling chamber	K
$T_{w,out}$	Water temperature at the outlet of the cooling chamber	K
T_{wv}	Water volume temperature	K
t_f	Shutdown time	s
t_i	Startup time	s
$t_{i,70\%}$	Time where 70% of the maximum combustion chamber pressure is reached	s
$\dot{U}_n$	Internal power	W
V	Volume	m^3
V_n	Nozzle volume	m^3
v_e	Exaust velocity	m/s
v_∞	Velocity of the fluid outside of the boundary layer	m/s

1. Introduction

A Hybrid Rocket Engine (HRE) is a thermo-chemical propulsion system that stores fuel and oxidizer in a multiple state of aggregation. Conventionally, the oxidizer is stored in liquid or gaseous form, whereas the fuel is solid. HREs feature multiple advantages with respect to the other thermo-chemical systems. With respect to Solid Rocket Motors (SRMs), the direct control on the oxidizer mass flow rate only makes them a simple throttleable system. Additionally, only the oxidizer requires a feeding system, reducing the complexity of the design compared to Liquid Rocket Engines (LREs). Thus, HREs promise simplicity, which contributes also to their cost-effectiveness, together with the ability to use cheap fuel formulations. All the considerations made above makes them an attractive propulsion system. However, traditional fuel formulations employed in HREs exhibit low regression rates and the propellants require an extended length for proper mixing. This results in HREs having a high length-to-diameter ratio (L/D) or more complex grain geometries to increase thrust, leading to structural challenges and reducing volumetric efficiencies [19, 26, 27, 29, 32]. Additionally, the diffusive flame in HREs leads to combustion efficiencies relatively lower than the other thermo-chemical combustion systems. These limitations have hindered the application of hybrid rocket propulsion systems in both launch and in-space scenarios.
The Vortex Flow Pancake (VFP) system represents an unconventional configuration for a HRE. It is originally proposed by Gibbon and Haag [11, 13]. In the VFP configuration, a tangential oxidizer injection generates a vortex flow field in the combustion chamber, formed within the gap between two solid fuel discs. The space between the two discs is smaller than their diameter, resulting in a compact engine characterized by a $L/D < 1$. The swirling flow created by this unique injection method results in improved mixing of the propellants (enhancing combustion efficiency) and providing at the same time thermal protection to the combustion chamber side walls thanks to the oxidizer flux, thus avoiding use of thermal protections systems. [11, 13, 15, 23, 25].
Furthermore, this innovative design drastically reduces the O/F shift phenomenon during combustion, which is a commonly observed drawback in traditional HREs [11, 15, 23, 25]
The Space Propulsion Laboratory (SPLab) at Politecnico di Milano has previously conducted experiments and is currently engaged in ongoing activities on its own developed SPLab Vortex Flow Pancake (SVFP). Research efforts are directed towards investigating different fuel formulations and the effects of operating parameters on fuel regression rates and combustion efficiency [14].
This research investigates the cooling process of SVFP engine's nozzle. The setup has a copper nozzle embedded in an aluminium cooling chamber where water can flow through. This design allows the nozzle to be used for multiple and longer firings without being subjected to significant erosion. However, the system by nature removes heat from the expanding gasses, thus influencing the performance of the engine. The research aims at understanding and characterizing the phenomenon through the analysis of data collected using a thermocouple and through the use of tools such as numerical modeling and CFD analysis.

1.1. State of the art

The determination of the combustion efficiency in hybrid rocket engines (HREs) is of paramount importance. The diffusion flame ruling the hybrid combustion and the burning mechanism yields relatively low combustion efficiencies, unless specific techniques are implemented as in Chapter 2 of Reference [19]. Vortex Injection of the oxidizer is a technique tackling the low combustion efficiency issue as discussed in [13, 18, 21, 23, 25, 28, 30, 35]. While beneficial in terms of regression rate enhancement and actual combustion efficiency increase, the tangential component of the swirl flow possibly affects the combustion chamber pressure readings of transducers as in Reference [21]. Thus, special attention in data processing is required [18, 21]. The effect on chamber pressure is mainly due to centrifugal effects induced by the vortex motion and implies a increase of the read value with respect to the actual one. Similarly, in lab-scale engines, the use of cooled nozzles requires detailed analyses for an evaluation of the propellant flow enthalpy losses induced by the heat transfer as reported in Reference [21] and [13].
To the best knowledge of the authors, the most comprehensive discussion of the aforementioned effects is given in Reference [13, 21]. In this latter work [21], Ozawa et al provide experimental data evaluating the enthalpy reduction in the propellant flow by the heat transfer to the nozzle. Thermocouple measurements were used to obtain a temperature history in the firing time. In the reference, data are considered in an effort for combustion efficiency determination by various methods. A similar effort is reported in Ref. [13]. In this latter work, Gibbon and Haag in Reference [13] provide an evaluation of the enhtpaly transfer from the combustion chamber of a VFP engine with water cooled nozzle. Some further comment on the results of Reference [13] reported in Chapter 9 where simplifying assumptions introduced by Gibbon and Haag are reported in details.
The aim of this work is to improve the series of diagnostics and data reduction methods implemented at SPLab to characterize the burning behavior and the performance of a VFP engine. The analysis will stem from previous works dealing with the determination of the influence on performance of the use of a water cooled nozzle.

Experimental lasting and numerical simulation are joined in an effort toward a detailed characterization of the VFP performance.

2. Experimental Setup

2.1. SPLab Vortex Flow Pancake

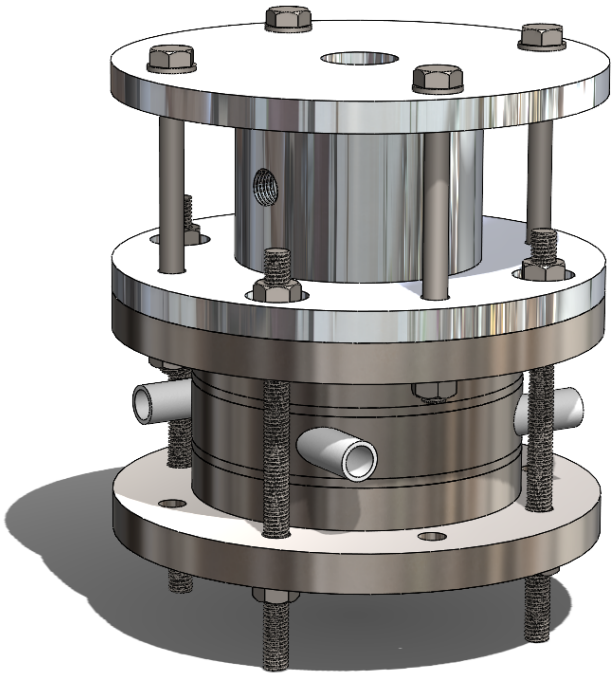

Figure 1: Vortex Flow Pancake motor combustion chamber and cooling chamber, CAD.

This chapter aims to provide readers with a comprehensive overview of the experimental setup used for the firing tests, comprising the engine test bench, the feeding system for coolant and propellant and the data acquisition system.
The Vortex Flow Pancake hybrid rocket engine in use at SPLab includes two flat solid fuel disks, each encased in an AISI-316 stainless steel ring. These two are separated by a tangential injection device with 4 oxidizer channels, used also for the final nitrogen purge, spaced along the circumference. The volume defined between the two fuel grains is the combustion chamber and it increases during the burning because of the regression of the two fuel disks. The entire assembly is held together by top and bottom connection flanges, with an O-ring gasket at each junction, and secured by four nuts and bolts. A convergent-divergent copper nozzle has been used, with $\varepsilon = A_e/A_t = 2$.
This nozzle is enveloped by a chamber used to cool it with water during the tests. Water flows through two pipes connected to the water pipeline system. This process inevitably results in some energy loss by the hot expanding gas mixture. However, this trade-off is deemed worthwhile as it significantly extends the nozzle's lifespan.

2.2. Test facility

The VFP facility is divided into two distinct areas. The first room houses the test bench, where the engine is fixed to a vertical sled. It is also equipped with a comprehensive array of testing tools and devices. This includes a pressure sensor mounted on one of the four injection arms, a second pressure sensor mounted axially to the chamber and opposite to the nozzle position (not depicted in Figure 3), a load-cell positioned in the direction of the thrust and an igniter that is connected to one of the four injection arms. The second room serves as the control center, equipped with a data acquisition unit and valves for opening and closing the flow of nitrogen, oxygen and water. The feed system is composed of two primary channels: the oxidizer line and

the nitrogen purge line, both operating under a feeding pressure of 4 MPa. These lines originate from the nitrogen and oxygen pressure tanks located in the engine room. From there, the feed lines extend into the control room, where the oxygen line is equipped with a manual valve ahead of the flowmeter for precise mass flow rate control. After passing through these components, the lines return to the engine room, connecting to the 4 engine injectors. Before the two separate lines merge together, a check valve prevents any hazardous back-flow and after the division, 4 electrovalves allow precise opening and closing just before of the combustion chamber. The Figure 2 shows the engine setup during a firing, while Figure 3 below is reported a comprehensive schematic view of the setup in use at SPLab.

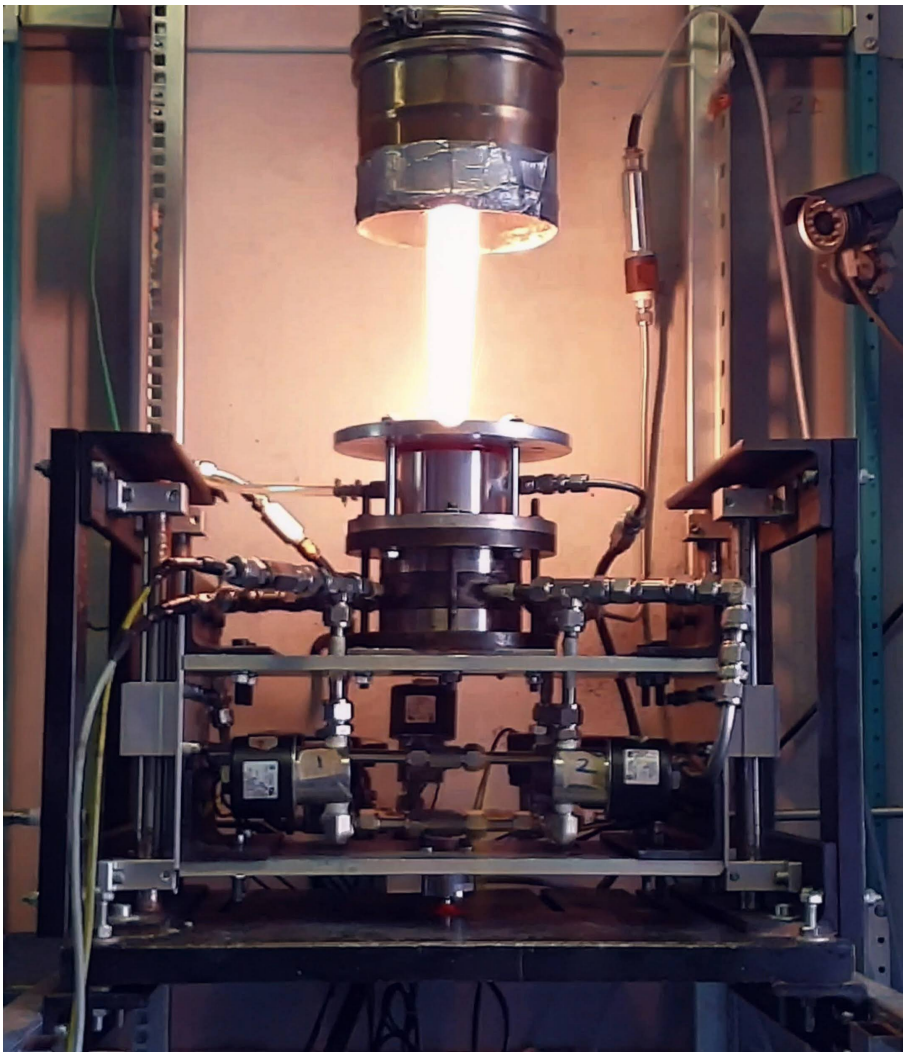

Figure 2: Vortex Flow Pancake motor during a test.

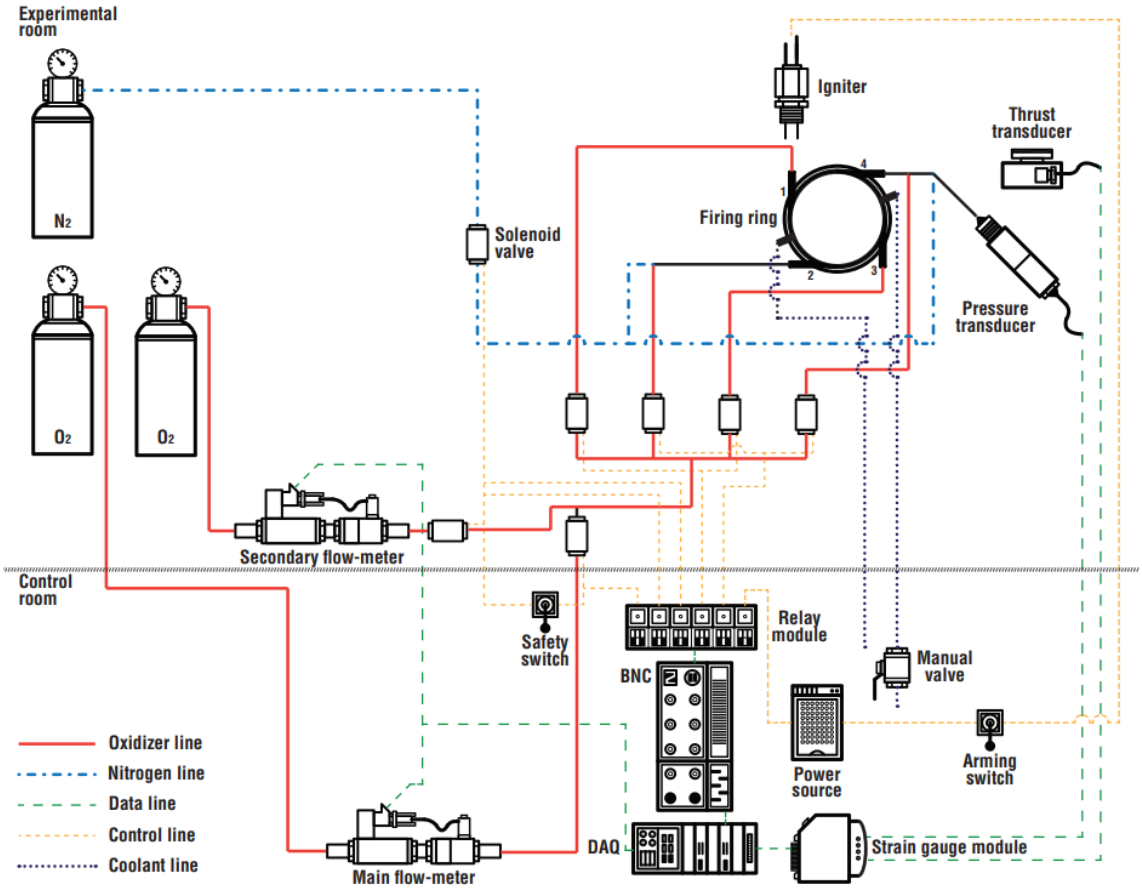

Figure 3: Vortex Flow Pancake motor experimental setup schematic [28].

3. Materials and Fuel Ingredients

The experimental tests in the laboratory were conducted using different fuel compositions, which can be grouped into two main categories: acrylonitrile-butadiene-styrene (ABS) grains and paraffin-based grains, characterized by different percentages of SEBS-MA and a fixed percentage of carbon powder. All the compositions are listed in Table 1.

3.1. ABS

ABS is a thermoplastic polymer used due to its mechanical and thermal properties, as characterized by Bisin et al. [9, 10], and its ease of shaping using 3D printing [9–11]. Its entalphy of formation is characterized by Whitmore et al. [31, 33], data required to compute the characteristic velocity in the NASA CEA code.

3.2. Paraffin

Paraffins belong to hydrocarbons' family, with the general formula C_nH_{2n+2}. At room temperature, they can exist in a liquid state if $10 \leq n \leq 18$ or in a solid state if $18 \leq n \leq 55$ [20, 34]. This latter category can be further divided into two primary groups: macro-crystalline ($18 \leq n \leq 30$) and micro-crystalline waxes ($40 \leq n \leq 55$). Macro-crystalline paraffin waxes exhibit greater malleability compared to the micro-crystalline type and possess a melting point within the range of $313 - 333$ K. On the other hand, micro-crystalline waxes present a more brittle behavior compared to macro-crystalline waxes and have a melting point within the range of $333 - 363$ K [20, 34].
The paraffin type utilized in this study is the SasolWax 0907, a commercial micro-crystalline paraffin wax, produced by Sasol GmbH [3, 4]. The brute chemical formula is $C_{50}H_{102}$ and serves as the primary component for the paraffin-based fuels formulations. Its high melting temperature of $356 - 367$ K and its low melt layer viscosity makes it a valid choice for hybrid combustion because it results in a good response to the entrainment effect.

By mixing paraffin with a certain percentage of Styrene-Ethylene-Butylene-Styrene grafted with Maleic Anhydride (SEBS-MA), a good balance is achieved between mechanical properties and the ballistic performance. Specifically, in this work, percentages equal to $5 - 10 - 20$ wt.% were used.

3.3. SEBS-MA

The SEBS-MA is a thermoplastic co-polymer that is commercially produced by Sigma-Aldrich [5]. In this work, it is used as a reinforcing additive to enhance the mechanical properties of the brittle paraffin matrix. Its mechanical and thermal properties, as well as its good compatibility with paraffin, make SEBS-MA an interesting reinforcing ingredient. The melting temperature range of SEBS-MA is $455 - 460$ K [7, 24].
The SEBS-MA chain consists of Styrene-Ethylene-Butylene-Styrene (SEBS) blocks that are grafted with 2 wt% of Maleic Anhydride (MA), which is linked to the butylene blocks. The central ethylene-ran-butylene block is responsible for the rubber-like properties of the polymer, while the two styrene blocks give SEBS its thermoplastic behavior. By adjusting the weight percentage of SEBS-MA in the blend, it is possible to tune the mechanical characteristics and ballistic results.

3.4. Carbon Powder

Carbon powder (CB) is a graphite micron-sized powder supplied by Sigma-Aldrich [5] and it is added to all paraffin-based compositions at a concentration of 1 wt%. Its presence offers multiple benefits, namely the enhancement of the of radiant heat transfer between the flame zone and the surface, while also preventing the thermal wave from penetrating the bulk of the fuel [24]. This would cause the degradation of the mechanical properties and sloughing of the fuel grain. The CB particles used have a diameter (ϕ) of less than 20 μm and a density (ρ) of 2.1 g/cm^3 [6].

Table 1: Tested formulations and theoretical maximum density.

ID	**ABS**	**Sasol 0907**	**SEBS-MA**	**CB**	**Density** ρ [kg/m^3]
ABS	100 wt.%	-	-	-	1050
W1	-	99 wt.%	-	1 wt.%	929
SEBS10	-	89 wt.%	10 wt.%	1 wt.%	928
SEBS20	-	79 wt.%	20 wt.%	1 wt.%	926

4. Fuel Manufacturing

4.1. ABS Grains

The ABS grains are obtained through fused deposition modeling (FDM) using filament provided by Prusa [1, 2]. The process is the following:

- model the grain geometry using a CAD software;
- save the geometry as a stereo lithography interface format (STL) file;
- upload the file to the software of choice, in this case *PrusaSlicer*, create and export the g-code file.

The creation of two disks and their insertion into the two metal hosting rings, will form the two regressing surfaces of the combustion chamber. The fuel disks used have an outer diameter of 86 mm and a central hole with a diameter of 25 mm, used to accommodate the carbon tube. The expected regression rate for ABS-GOX is 0.24 mm/s (from previous tests in SPLab [30]), and the maximum test duration is 15 seconds, so a height of 3.6 mm for the two disks would be sufficient. To provide a safety margin and residual rigidity, a height of 7 mm is used, and supports were employed to achieve an initial combustion chamber height of 20 mm.

4.2. Paraffin-based Grains

The process leading to the creation of paraffin-based grains differs from that used for ABS. For all formulations, the procedure remains the same, with only the percentages of ingredients and mixing parameters varying. The raw materials are melted and subsequently solidified to achieve a cylindrical shape, and for this purpose, 3D-printed molds made of polyethylene terephthalate glycol (PETG) are used.
These molds are printed to be larger than necessary to account for material shrinking (approximately $15-25\%$ of the volume) and subsequent metal case fitting manipulations. Below, the procedure for creating the blends is presented.

- The first ingredient is paraffin. It is placed inside a glass beaker, which is then positioned within an oil bath. The oil is gradually heated using a hotplate until it reaches the desired temperature, which, in this case, falls within the range of 393-433 K. This specific temperature range is chosen to prevent the evaporation of lighter paraffin wax fractions while facilitating complete melting. Once complete melting is achieved, the subsequent step can be performed.
- Once the paraffin has completely melted, the first ingredient to be incorporated is SEBS-MA, for the production of grains with improved mechanical properties. The dissolution of SEBS-MA is a time-consuming process, requiring 5 hours for SEBS5, 7 hours for SEBS10, and 11 hours for SEBS20 [12, 22]. It is crucial during this phase not to exceed a temperature of 453 K to prevent the breakage of -MA bonds within the molecule [7]. To facilitate the effective blending of paraffin and SEBS-MA while preventing the formation of clusters, an electric impeller with a helical design is used.
- Before the addition of the carbon powder, is important to reduce the hotplate's temperature and allow the blend to gradually approach the solidification temperature for increased viscosity. This method results in a denser mixture and prevents the carbon powder from settling. During this process, the impeller remains active, ensuring the uniform dispersion of the carbon powder.
- After achieving a good dispersion of the carbon black (which takes a few minutes), the beaker is removed from the oil bath, and the blend is carefully poured into the molds manually. At this point, the molds are covered with their caps, which, by applying a constant pressure, partially prevent shrinking. Before proceeding with the removal of the grains, it is necessary to wait at least 5 hours to allow for complete solidification.

After the grains have solidified, the extraction and mechanical processing can be carried out. The grains will need to be processed with a drill to create the central hole and with a lathe to remove excess material to ensure the fitting into the metal cases, with nominal diameters coinciding with the ones reported in ABS. Figure 4 is a picture of produced fuel grains.

(a) (b)

Figure 4: Fuel grains: (a) ABS and (b) Paraffin-based.

5. Experimental Procedures

The procedure for a standard combustion run is detailed below, highlighting the crucial steps. The process begins with a pre-firing test, which includes the preparation and assembly of the engine on the test bench. This is followed by the firing test. Once the test is completed, the engine is disassembled, data is gathered, and post-processing is carried out.
The assembly process kicks off in the workshop with an inspection of the engine in readiness for the test. The first step involves inserting the NO and N2 fuel grains (NO and N2 denote the nozzle side and bottom side of the engine respectively) into their corresponding metal rings. These grains are then weighed and key dimensions

for post-processing are measured using a caliper, specifically six disk height and diameter measurements of the central hole.
In addition to the two disks, the weights of the two segments of the carbon tube, which are to be inserted into the central hole of the two fuel grains, are also recorded. These carbon tubes play a crucial role in preventing the combustion of the sidewall adjacent to the inner holes, while the outer perimeters are safeguarded by the metal rings.
After these tasks are completed, the NO side disk and its corresponding carbon tube are meticulously positioned and firmly secured in their assigned spot within the upper section of the motor, which includes the nozzle and cooling chamber. The assembly should ensure contact between the carbon tube and the nozzle, and a gasket between the fuel disk and nozzle block guarantees pressure sealing once the bolts are tightened. Following the insertion of the N2 carbon tube into the N2 disk, these components are transported to the firing site.
The N2 disk and the NO disk are coupled with the injector ring and the entire assembly is secured to the moving sled using four bolts. Both the inlet and outlet water pipes are connected to the cooling chamber. A thermocouple is connected to the outlet water pipe to monitor the temperature at the exit. The pressure sensor is linked to injector 3 in Figure 3, and the igniter is connected to the diametrically opposed injector 1, facing each other. A second pressure sensor is linked to the bottom of the engine in a central position to detect pressure data unaffected by centrifugal action. In the Figure 3 scheme the second pressure sensor is not marked.
The igniter used is made up of a small quantity of HTPB-AP-based solid propellant, which is applied to a Kanthal wire. This wire is heated with a 12 VDC power source to initiate ignition. After the engine has been fully assembled, the platform can be lifted off the support blocks and positioned on the load cell.
At this point the manual valves of the pipelines and both the N_2 and O_2 tanks are opened grant the gas flow to the SVFP up to the electrovalves. Then, the chimney is opened to allow the exhaust gases to exit, two ventilation fans are activated and the room is closed. As a safety measure, the operational procedures from this point on are carried out from the adjacent room visible in Figure 3.
In this room, the flowmeter is turned on and it must reach the operating temperature before the firing test starts. This process typically takes around 25 minutes. The data acquisition system is turned on and connected to flow-meter, pressure sensor, load-cell, electrovalves and igniter. All the operations required to conduct the test are set manually prior to the test and then performed by the computer running LabVIEW® system once the start button is pressed.
After opening the water valve for the cooling system, the oxygen mass flow rate is gradually increased until it reaches the desired value. At this point, the temperature values of the water at the outlet and the pressure values inside the engine are checked to ensure the correct functioning of the sensors.
The test can begin and is carried out for a certain duration. The entire test is monitored from the control room through two monitors: one connected to a camera looking at the engine, and the other with the LabVIEW® control panel open.
Once the preset burning time is reached, the oxygen electrovalves are closed, and the nitrogen electrovalves are opened, in order to stop the combustion, cooling the nozzle, and purging the system.
After the test is concluded, the operator enters the test room. The igniter is unplugged, and the oxygen and nitrogen tanks are closed. The engine is lifted from the load cell before proceeding with the disassembly.
The next part of the procedure takes part back in the workshop, where the fuel disks and carbon tubes weights are re-measured, and their final mass is registered. Finally, the grains are removed from the metal rings, and the rings are cleaned for reuse.

6. Firing-Data processing

During the test, all the data regarding pressure, oxygen mass flow rate, thrust, and temperature are saved in four or five *.txt* files, depending on the number of pressure sensors used. Data processing is performed using MATLAB® by importing the *.txt* files as matrices where the first column contains time instances in seconds, while the second column contains the values of the quantities of interest.
Once all the files are saved within the same folder, loading the pressure trace file into the MATLAB® script will make it recognize whether a single or dual pressure transducer are being used and make it load all the remaining files of that given test.
The Fourier transform of the signal is computed, and upon observing the characteristic frequencies, the decision is made to use a low-pass filter. This filter allows for the retention of small oscillations caused by combustion instability while simultaneously eliminating oscillations due to instrument noise. The challenge with this approach arises when using a low cut-off frequency, as it may result in the removal of certain signal peaks that are still of interest. Conversely, if the cut-off frequency is too high, there is a risk of obtaining a filtered signal that is excessively noisy.
To address this issue, it has been determined to employ a relatively low cut-off frequency and, subsequently, to reintroduce any removed peaks. This is achieved through a comparison between the filtered trace with the

low-pass filter and the original trace. If the absolute value of the difference between the two exceeds a certain threshold value, the corresponding segment of the original trace is replaced in the filtered trace.

6.1. Pressure

Before proceeding with the filtering of the pressure trace, the graph of the pressure raw data is plotted. From this, the final instant of combustion t_f, namely the one just before the pressure peak caused by the nitrogen purge, is observed. The initial instant of the burning test $t_{i,\,70\%}$, is the moment associated with the attainment of 70% of the maximum pressure of a clean trace, that should be properly filtered to remove undesired spikes associated to noise or instabilities. These two instants in time define the combustion window, which is used for the calculation of average quantities, under the reasonable assumption of no significant time delays between thrust, pressure and mass flow rate traces. The filtered pressure plot with the starting and ending instants of firing is shown below in Figure 5. In the figure can be appreciated that at time $t = 12$ s the oxygen valves open and the flow-meter does the same gradually until the flow rate previously set is reached. At time $t = 35$ s there is ignition and at time $t = 50$ s the nitrogen valves open, extinguishing the flame and purging the system.

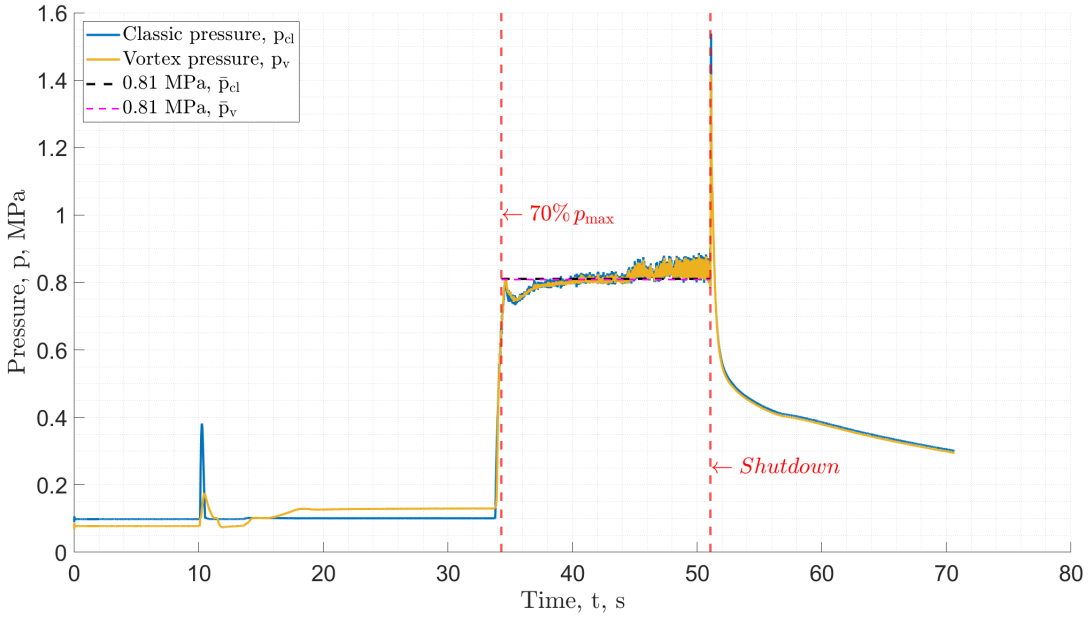

Figure 5: Filtered pressure traces of dual pressure sensor firing, where time 0 is the start of the test.

The average pressure is calculated as:

$$p_{avg} = \frac{1}{\Delta t_b} \int_{\Delta t_b} p(t)\, dt \tag{1}$$

Where the burning time is computed as $\Delta t_b = t_f - t_{i,\,70\%}$.
The pressure trace comes from a sampling frequency of 3000 Hz and the low-pass filter has been applied with a cut-off frequency of 120 Hz to obtain a trace clean from noise, along with a band pass filter between 40 Hz and 90 Hz to reintroduce occasional peaks. All the visible oscillations are due to the combustion process. The central pressure sensor is added to the setup with the aim of highlighting any differences between the pressure calculated in this point (p_v) and the pressure subjected to the centrifugal effects of the vortex (p_{cl}). As can be seen in the Figure 5, there are no significant differences between the two pressure traces.

6.2. Thrust

For the calculation of thrust, it is necessary to subtract the weight of the engine from the value measured by the load cell.

$$T(t) = T_{measured}(t) - T_{static} \tag{2}$$

The T_{static} has been computed using the first 9 s of the acquisition window, where no other operations are performed to allow the zeroing, otherwise the thrust measurement would be offset of the engine's weight.

$$T_{static} = \frac{1}{\Delta t_{static}} \int_{\Delta t_{static}} T_{measured}(t)\, dt \tag{3}$$

The average thrust is then computed as:

$$T_{avg} = \frac{1}{\Delta t_b} \int_{\Delta t_b} T(t)\, dt \tag{4}$$

where Δt_b is taken from the pressure trace. Similar to the pressure data, the thrust sampling frequency is 3000 Hz and the filtered trace is obtained using a low-pass filter with a cut-off frequency of 120 Hz together with the same band pass filter allowing frequencies between 40 Hz and 90 Hz to describe the combustion instabilities. An example of thrust trace is shown in Figure 6.

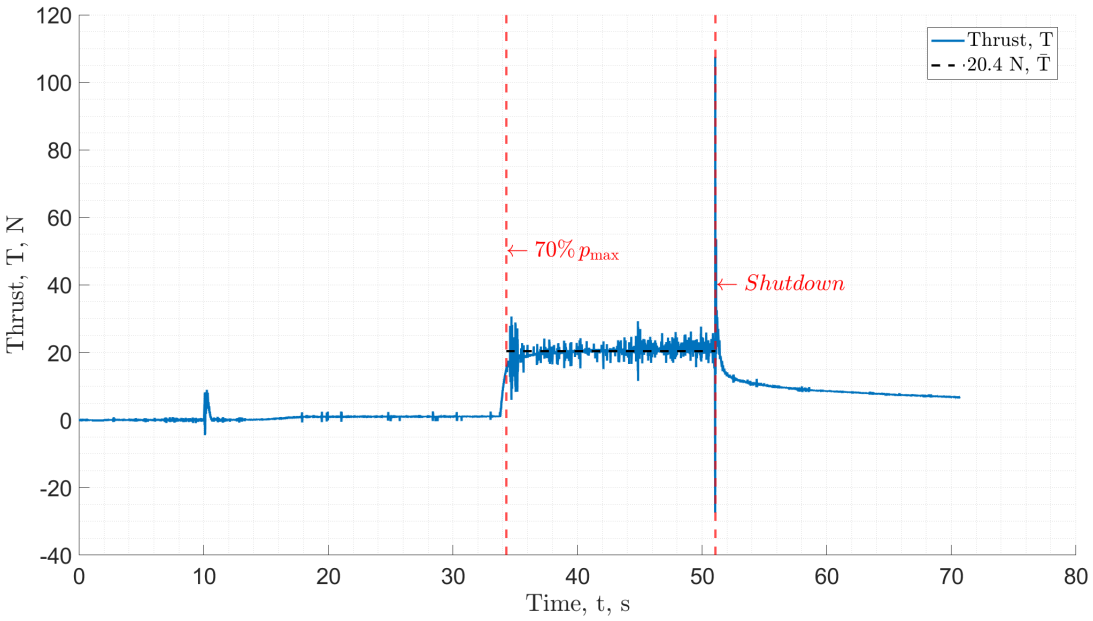

Figure 6: Filtered data of thrust.

6.3. Oxidizer Mass Flow Rate

The analysis of the oxidizer mass flow rate data did not require the use of a filter. This is because, unlike the pressure and thrust traces, the data collection frequency from the device is 3 Hz. This low frequency forces the use of the raw data, given the limited number of data points available (for a 15 s firing, there are only 45 data points). The burning window is taken from the pressure trace, and the average mass flow rate is computed as:

$$\dot{m}_{ox,avg} = \frac{1}{\Delta t_b} \int_{\Delta t_b} \dot{m}_{ox}(t)\, dt \tag{5}$$

Oxidizer mass flow rate plot is shown in Figure 7.

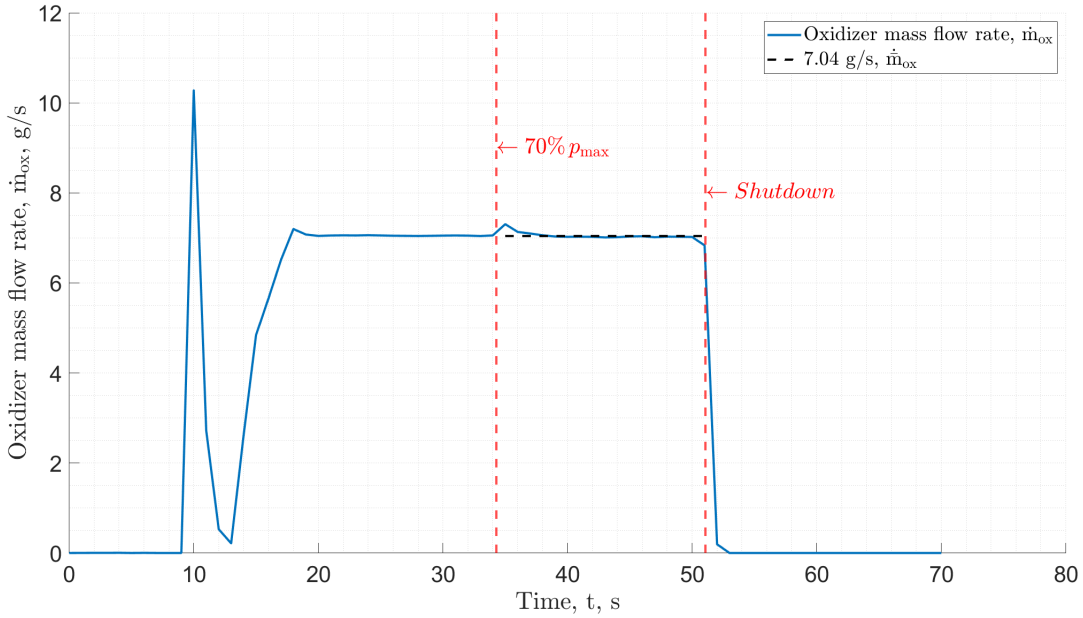

Figure 7: Filtered data of oxidizer mass flow rate.

6.4. Temperatures

Given that this work is focused on evaluating temperatures and losses due to cooling, the analysis of temperatures requires a more detailed and specific study and data goes through a specific filtering process. In this case, the data comes from a thermocouple, located at the outlet of the cooling chamber, with a sampling frequency of 1000 Hz. The transition from the time domain to the frequency domain is achieved through a Fourier transform. Subsequently, the temperature trace is filtered using a low-pass filter with a cut-off frequency of 0.3 Hz Figure 8 below illustrates an example of a water temperature curve.

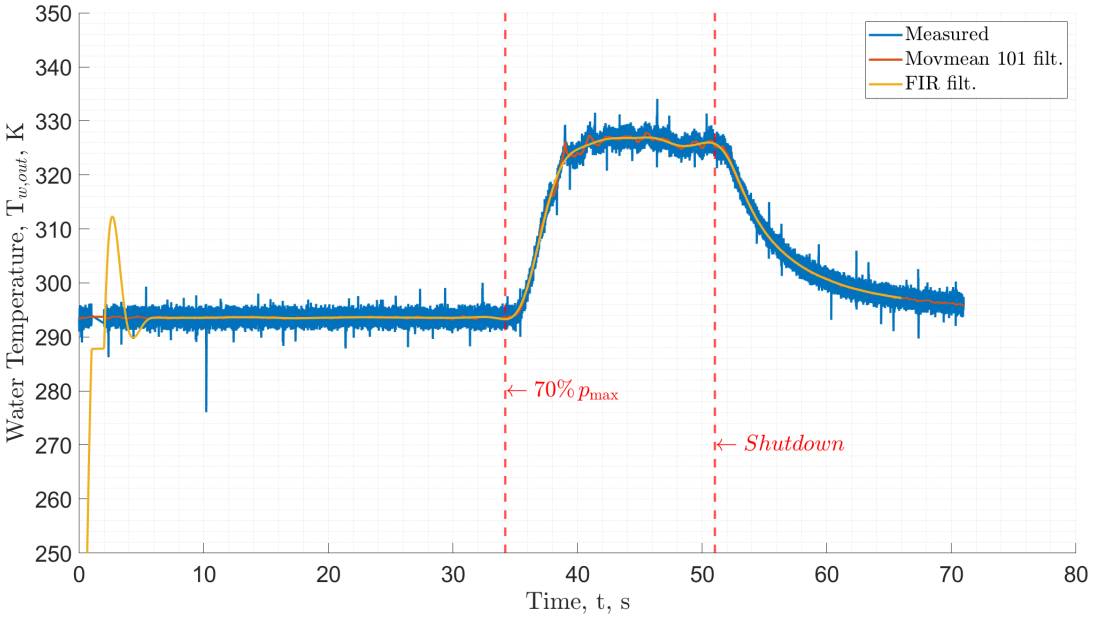

Figure 8: Example of water temperature trace.

The plot includes a *movemean* smoothed trace used in the former iteration of the code. However, this filter was later discarded due to the irregularity of the first-order derivative, which caused significant issues in calculating the nozzle temperature. The finite impulse response (FIR) filter introduces an initial oscillating part, observable

in Figure 8 and 9 as well as a delay of the whole trace which can or cannot be negligible, based on the filter order and the data availability. Since temperature data beyond the end of the combustion are available but not of significant interest, the whole trace can be translated to get rid of this shift, as visible at the end of the trace of Figure 8 and 10. Particular attention must be made on not losing data inside the burning window and to shift back the temperature trace of the delay introduced by the filter.

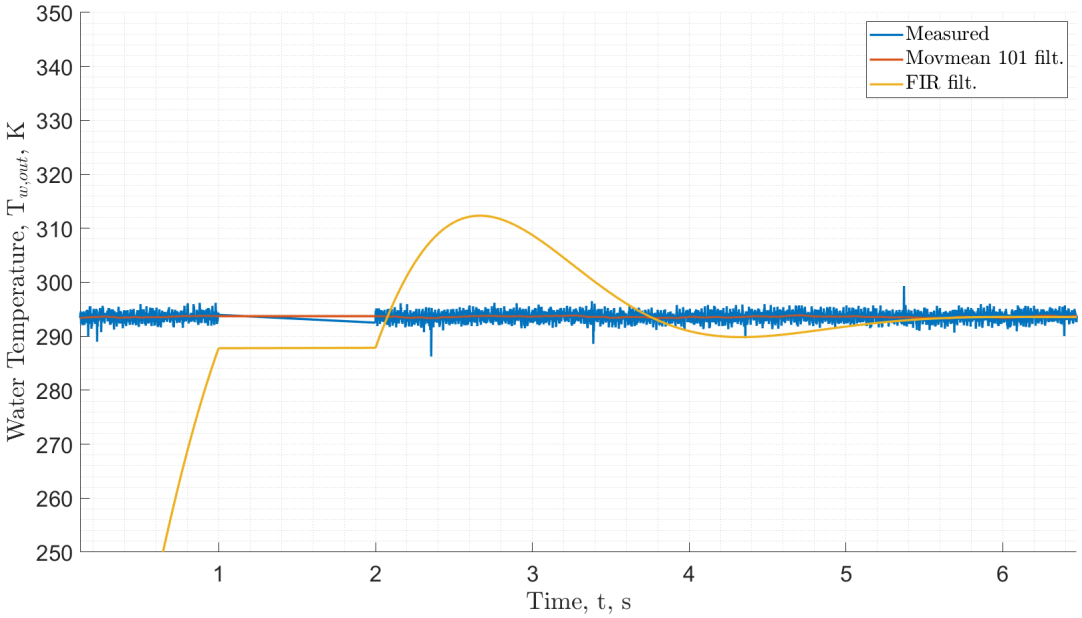

Figure 9: Effects of the FIR: initial oscillation.

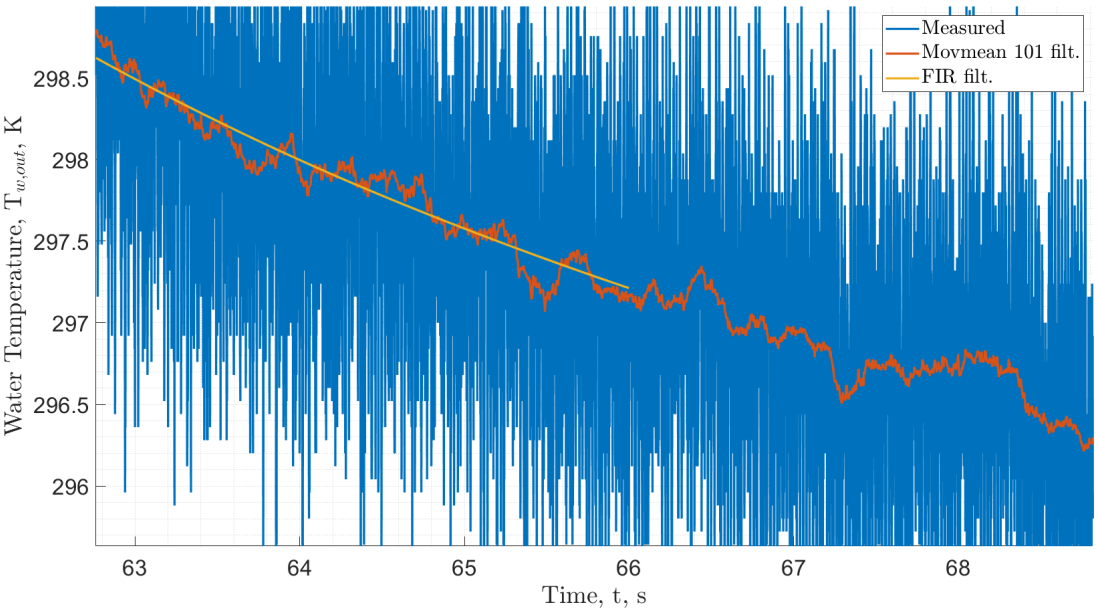

Figure 10: Effects of the FIR: time delay and loss of data after translation.

7. Thermal analysis

The following chapter will delve into the formulation of the thermal model capable of describing the problem, together with its implementation in the form of a MATLAB® code and the CFD analysis performed as a mean of verification and validation of the thermal model constructed. Before proceeding with the description of the

thermal model, is important to understand the cooling system setup, that can be seen in the exploded view in Figure 11. The nozzle is enclosed in an aluminium chamber composed of a cylindrical wall, sealed at both ends by two flanges secured one to the other with four pairs of bolts and screws. To provide a watertight fit and thermal decoupling between the nozzle and aluminium case, all the components are sealed with thermal paste and o-rings. The sides of the cylinder have two holes, where the inlet and outlet for the water cooling circuit are connected. The complete thermal problem, from the inside to the outside, can be sketched as:

- heat convection between the exaust gases and the nozzle internal surface;
- heat conduction inside the bulk material of the nozzle;
- heat convection between the outer surface of the nozzle and the water inside the chamber;
- heat convection between the water and the aluminium sides of the cooling chamber;
- heat convection between the ambient air and the cooling chamber assembly.

The conduction in the two contact points between the cooling chamber and the nozzle is prevented by the presence of insulation paste and O-rings which grant adiabaticity. Also, during transients heat accumulation is accounted for.

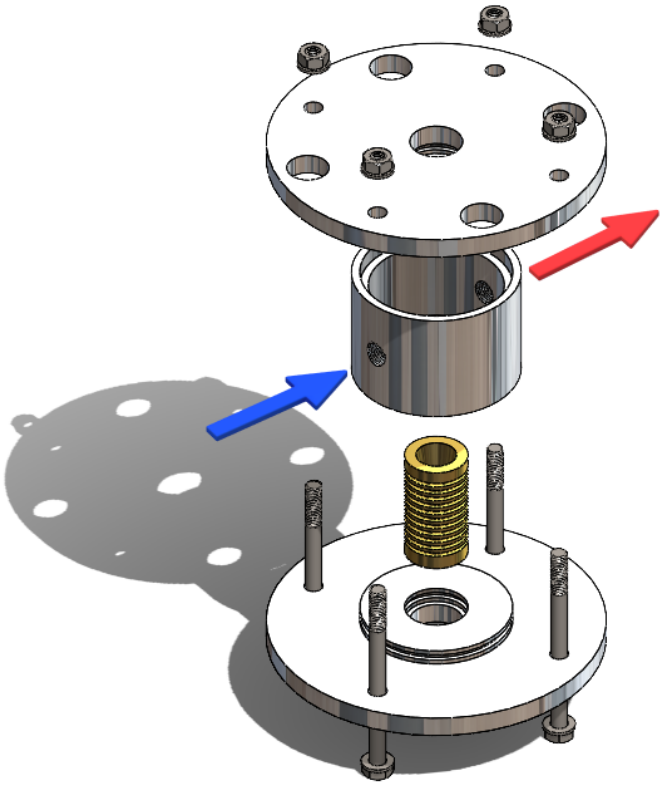

Figure 11: Exploded view of the nozzle cooling chamber assembly, where the arrows represent the cold water going in water and hot one coming out.

For the formulation of the thermal model is important to have a clear view of the physical variables that need to be modeled in order to critically reduce the problem as much as possible to limit errors and complexity. The aim is obtaining an evaluation of the heat flux leaving the combustion products and therefore not contributing to the generation of thrust via the gas-dynamic expansion. The only empirically measured experimental quantity is the water temperature, which is the mean through which most of the heat is brought away from the nozzle. Significant amounts of energy might also be stored inside the nozzle itself or the aluminium case and therefore requires a study to determine the temperature evolution of the system. The theoretical model of the problem is thus presented in the following section.

7.1. Thermal problem

A first idea of the thermal behaviour is suggested by the measured water temperature exiting the cooling chamber, of which an example is reported in Figure 8. During the firing, a plateau is reached after ≈ 5 s seconds after a ramping. This is very important because one might think to immediately simplify the problem considering a steady state condition. However, considering firing duration between 7 and 20 seconds how it is in this work,

the transient period of 5 s would represent between 25-70 % of the total period. Therefore, it cannot be ignored and transient must be included in the problem. However, the model can be simplified somewhere else.
A first simplification of the problem regarding the decoupling of the top and bottom flanges of the cooling chamber from the nozzle can be made because of the insulating layer and O-ring separating the two. In this way the whole nozzle is subject only to the heat exchange with the water on one side and the hot gases on the other.
A second simplification regards the water-cooling chamber walls system. Looking again at the exit water temperature evolution, the maximum achievable temperature difference between the two is the difference between the peak water temperature depicted in Figure 8 and the ambient temperature. This, along with the fact that the two exchange by free convection and that free air heat transfer coefficient is two orders of magnitude smaller than the water one results in a theoretical maximum heat of some order of magnitudes lower than water-nozzle. Thus, it can be treated as 0 and not modelled. The immediate consequence of these considerations is the possibility to neglect the cooling chamber-air heat exchange.
The third simplification made is to not treat the fins as distinct elements but to consider them as an equivalent surface of the nozzle. This has come from preliminary calculations based on fin models of Reference [8], which revealed a ninety percent efficiency of the fins due to their short overhang.
The last consideration to be made at this stage is the one regarding water and nozzle, which are approximated as two single nodes at uniform temperatures as well. For the water volume this hypothesis has a minor impact due to both the low temperature gradient and to the compensation derived from algorithm tuning through more accurate CFD analysis. Regarding the nozzle, however, more words must be spent on the decision made, therefore the discussion will be reprised in Section 9.1.

At this point, a simplified transient problem is obtained in which all the heat removed from the exhaust gases is or removed by the water flow or accumulated in the nozzle. Energy balance at nozzle leads to:

$$|\dot{Q}_{gas}| = \dot{Q}_n + \dot{Q}_{wv} \tag{6}$$

where $\dot{Q}_n$ is the power absorbed by the nozzle and $\dot{Q}_{wv}$ is the power absorbed by the water.
The first can be calculated according to the heat gain theory as:

$$\dot{Q}_n = \dot{U}_n = \rho_n V_n c_{p,n} \frac{\partial T_n}{\partial t} \tag{7}$$

where $\dot{U}_n$ is the internal power, ρ_n is the density of the metal of which the nozzle is made, V_n is its volume, $c_{p,n}$ is the specific heat and $\frac{\partial T_n}{\partial t}$ represents the nozzle temperature variation with time.
The second member of Equation 6 is computed through the Newton's Law of Cooling [8]:

$$\dot{Q}_{wv} = h_{wn} A_n (T_n - T_{wv}) \tag{8}$$

where $\dot{Q}_{wv}$ is the heat power transferred from the nozzle to the water voume, $T_{wv} = (T_{w,in} + T_{w,out})/2$ is the water core volume temperature obtained as average of the inlet temperature and the outlet temperature, h_{wn} is the generic convective heat transfer coefficient, A_n is the interface surface between nozzle and water and therefore set as the nozzle external surface comprising of the fins area. T_n is the solid wall temperature, but coincide with the bulk temperature due to the single node approximation.
Centering the point of view in the water volume, the power going into the coolant can be expressed also in the following way:

$$\dot{Q}_{wv} = \dot{m}_w c_{p,w} \Delta T_w \tag{9}$$

where $\Delta T_w = T_{w,out} - T_{w,in}$ is the difference between the inlet water temperature and the outlet water temperature, $\dot{m}_w$ is the water mass flow rate and $c_{p,w}$ is the specific heat of water.

The complexity of the convective interaction is contained in the coefficient h_{wn}, since varies a lot as function of the chosen model for the convective transfer. The approach used to model h_{wn} is to employ an empirical formulation for calculating the Nusselt number and then determining the corresponding convective parameter. Therefore, it is necessary to understand the fluidynamics inside the cooling chamber in order to choose the most appropriate model. A prelimary CFD study highlighted a velocity distribution difficult to classify, with a mixed behaviour between free convection (top and bottom part of the chamber) and cylinder in cross flow in the central part identified by the water injection axis and the nozzle normal plane. Due to this specific velocity field, literature lacks correlations suitable for calculating the Nusselt number. Thus, free convection model and cross flow model were implemented in a mixed discretized approach.
To study the interaction between the nozzle and the jet, an expression for a cylinder in cross-flow has been employed. The following is a function proposed by Churchill and Bernstein [8] that covers a wide range of

Reynolds and Prandtl numbers, in particular the equation is recommended for all $Re_D Pr \geq 0.2$ and has the form:

$$\overline{Nu_D} = 0.3 + \frac{0.62 Re_D^{1/2} Pr^{1/3}}{[1 + (0.4/Pr)^{2/3}]^{1/4}} \left[1 + \left(\frac{Re_D}{282000} \right)^{5/8} \right]^{4/5} \tag{10}$$

where Nu_D is the average Nusselt number and D is the characteristic length, that in this case of a cylinder in cross flow is represented by its diameter.
The Reynolds and Prandtl numbers are defined as:

$$Re_D = \frac{\rho_w v_\infty D}{\mu_w} \tag{11}$$

$$Pr = \frac{c_{p,w} \mu_w}{k_w} \tag{12}$$

where D is again the characteristic length of the nozzle as in Eq. (10), ρ_w, k_w, μ_w and $c_{p,w}$ are the fluid (thus water) density, conductivity, viscosity and specific heat, while v_∞ is the fluid velocity outside the boundary layer.

For the second model, a correlation typical for free convection interaction has been used. The expression used is the one recommended by Churchill and Chu in Reference [8], which provides the average Nusselt number over the entire circumference of an isothermal cylinder.

$$\overline{Nu_D} = \left\{ 0.60 + \frac{0.387 Ra_D^{\frac{1}{6}}}{[1 + (0.559/Pr)^{\frac{9}{16}}]^{\frac{8}{27}}} \right\}^2 \tag{13}$$

Where Ra_D and Gr are the Rayleigh and Grashof numbers, respectively, whose expressions are given below, considering the external nozzle diameter as characteristic dimension:

$$Gr_D = \frac{g \beta (T_n - T_{wv}) D^3}{\nu_w^2} \tag{14}$$

Here g is the gravity acceleration, $\beta = \frac{1}{T_{film}} = \frac{1}{T_{wv}}$ is the thermal expansion coefficient, T_n is the wall temperature, T_{wv} is the water volume temperature, D is the characteristic length and ν_w is the kinematic viscosity.

$$Ra_D = Gr_D Pr \tag{15}$$

where Pr is the same of Eq. (12). This correlation for the Nusselt number is valid for wide range of Rayleigh number, in particular $Ra_D \leq 10^{12}$.
All the foregoing correlations are evaluated using the thermophysical properties calculated at the average temperature between the incoming water and the water exiting the cooling chamber, as the temperature used in the Eq (8).
The Nusselt number is defined as ratio between convection and conduction heat transfer in the fluid:

$$Nu = \frac{h_{wv} D}{k_w} \tag{16}$$

where h_{wn} is the convective coefficient, D is the characteristic length and k_w the water thermal conductivity. The two models lead to two convective coefficients, h_{Free} related to the free convection and h_{Forced} related to the cross-flow.
Let's now define α as the unity fraction of the nozzle height on which the water jet impacts.
The $\dot{Q}_{wv}$ of Eq. (8) can be redefined as sum of the two contributes:

$$\dot{Q}_{wv} = h_{wn} A_n (T_n - T_{wv}) = h_{Free} (1 - \alpha) A_n (T_n - T_{wv}) + h_{Forced} \alpha A_n (T_n - T_{wv}) \tag{17}$$

Thus, simplifying, the whole nozzle convective coefficient can be written as weighted sum of the free-convection and cross-flow convection

$$h_{wn} = (1 - \alpha) h_{Free} + \alpha \, h_{Forced} \tag{18}$$

where $0 \leq \alpha \leq 1$ shall be determined.

7.2. Numerical formulation

The thermal model previously described is adapted into an algorithm capable of solving the water volume temperature, nozzle temperature, the various heat powers. The code is developed in the MATLAB® environment. In the first part of the code, the outlet water temperature trace measured by a thermocouple $T_{w,out}$ is imported. The temperature trace is filtered as explained in Section 6.4. The FIR filtered temperature profile is the starting point for calculating the nozzle temperature. Thermophysical properties of water and the materials used in the cooling chamber are given as input as well and taken from Ref [8]. The tabulated properties function of temperature are then interpolated using a polynomial function. Water properties and copper properties are shown in Figure 12 and 13.
The first part of the problem is based on solving T_n from the double definition of $\dot{Q}_{wv}$ in Eq. (8) and Eq. (9), which results in:

$$\dot{m}_w c_{p,w}(T_{w,in} - T_{w,out}) = h_{wn} A_n (T_n - T_{wv}) \tag{19}$$

$T_{w,in}$ is the temperature of the cold water entering the cooling chamber and is assumed constant in time. It is computed as an average of values recorded by the thermocouple in exit from the cooling chamber in the period of the test before the ignition. T_{wv} is the temperature of the water volume inside the chamber and is computed at every instant as the average of the cold and the hot side, as indicated in Eq. (8). Thus, $c_{p,w}$, function of $T_{w,out}$ is known in time as well and the only unknown remains T_n. However, the equation is implicit since the heat transfer coefficient h_{wn} is function of T_n and cannot be analytically solved, as can be seen from the formulations in Chapter 7. To obtain a fast algorithm, a specific solver is designed on a matrix based approach. The calculation of the nozzle temperature is performed by constructing a T_n guess matrix of size $N \times M$, where the M columns span every time step and the N rows contain the guess temperatures associated to the column/time instant. These temperatures range from $T_{w,in}$ in the first row to 1373 K (copper melting temperature) in the last row, with step of $step\_0 = 10$ K. Interfacing matrices are built also for the other terms of the equation, where their $1 \times M$ vectors (values in time) are copied in N rows to match T_n matrix size. h_{wn} is thus computed as $N \times M$ matrix from the T_n guess matrix. At this point, the matrices are used to solve the Eq. (19) for T_n, resulting in a new matrix of nozzle temperatures. The next step involves calculating the absolute difference between the initial matrix of guessed nozzle temperatures and the one calculated. The $1 \times M$ indexes associated to the smallest deviation between the estimated and calculated temperatures for each row, and therefore time, are isolated. This leads to the creation of a new estimate $21 \times M$ matrix, where the vector of guess nozzle temperatures corresponding to the elements with the smallest deviation for each time instant is positioned in the central row and the rest of the cells are filled with values above and below the central one spanning the range of temperatures of the previous guess matrix with a step that is one tenth the previous one: $step\_k = 0.1\ step\_(k-1)$ (e.g. $step\_1 = 0.1$ K if $step\_0 = 1$ K). Algorithm is iterated until the maximum of the $1 \times M$ deviation vector at the k iteration is below the desired tolerance. This matrix formulation of the problem, even if more articulated with respect to using cycles, allowed a much faster computation time and most importantly does not suffer from convergence problems.
Once the nozzle temperature is known, its derivative, necessary for Eq. (7), can be computed using the central finite difference method:

$$\left.\frac{\partial T_{noz}}{\partial t}\right|_i = \frac{T_{i+1} - T_{i-1}}{2\Delta t} \tag{20}$$

A good FIR filtering performed on the empirical data allowed to obtain a smooth nozzle temperature derivative. Now, both $\dot{Q}_{wv}$ and $\dot{Q}_n$ of Eq. (7) and Eq. (9) for every time instant can be computed in equation form. This way of expressing it allows to use the correct properties for water and copper at a given temperature. The water mass flow rate $\dot{m}_w$ in Eq. (9) and nozzle volume V_n in Eq. (7) are one measured empirically and the other extracted from the CAD model. The total heat is then calculated as in Eq. (6).
Preliminary runs of the code using full cylinder in cross flow (α=1) formulation and a first approximation of the flow velocity at half of the injection speed returned a first guess of nozzle temperatures.
Precisely, there are still three variables in the code which requires further analysis:

- water jet velocity for the forced convection model used to compute the dimensionless numbers expressed in Section 7.1 which must be comprised between 0 and the velocity in the feeding tube;
- fraction of the nozzle (α) exposed to the jet as defined in Eq. (17);
- a correction factor for the heat transfer coefficient λ capable of accounting for all the uncertainties in the formulation that is adapted from existing models which might require a correction based on the results of this specific application.

The formulation of precise values for the variables described above is a matter requiring further study and is reprised in Section 7.4 after a comprehensive CFD study reported in Section 7.3.

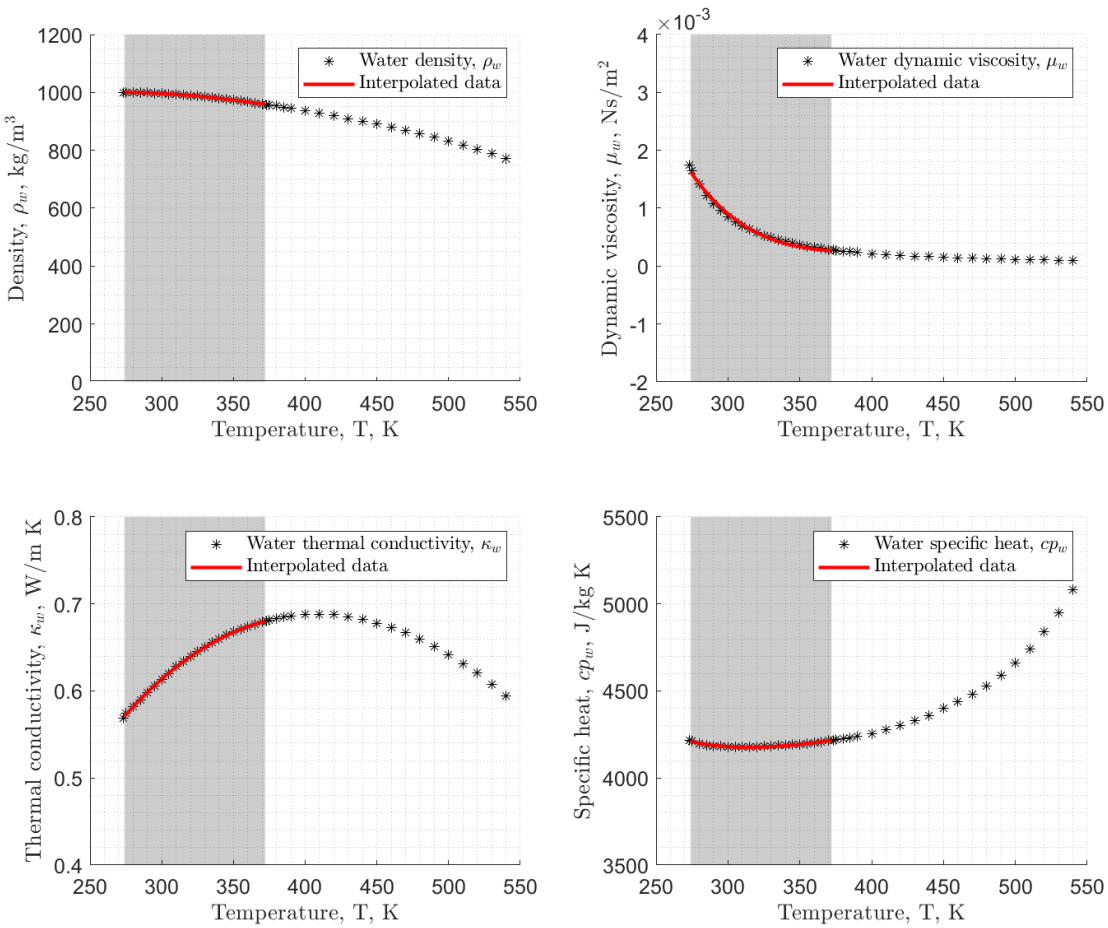

Figure 12: Water properties.

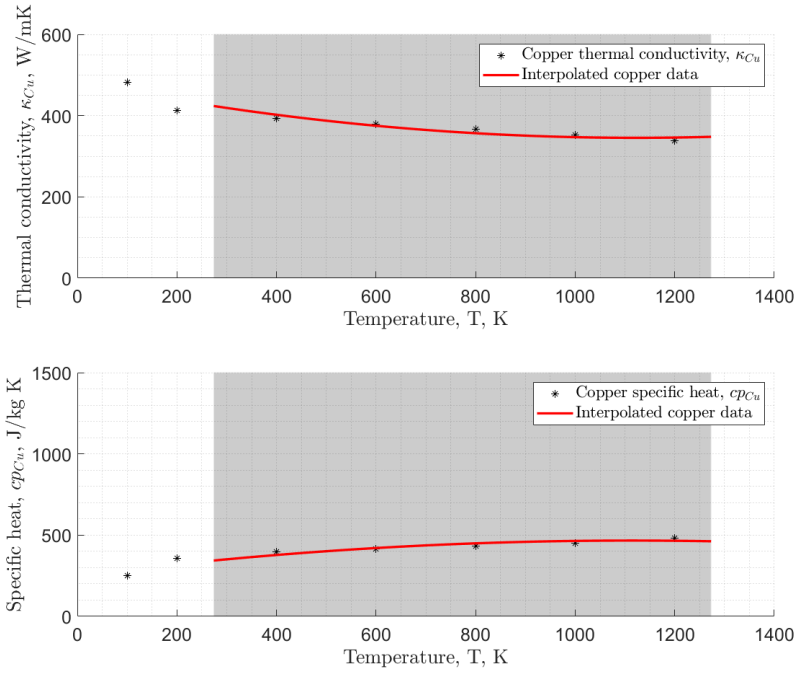

Figure 13: Copper properties.

7.3. CFD analysis

By using Computational Fluid Dynamics (CFD) correctly, it is possible to simulate complex problems such as the coupled thermal-fluid dynamics of interest. The CFD is a powerful tool that when combined with experimental data can give a correct and detailed view of the system. In this work it is important for the comprehension of the fluid dynamics inside the cooling chamber and therefore for the selection of water jet velocity and α. The thermal analysis can provide a value for λ. The objective of this chapter is to present the workflow followed for the thermal-fluid dynamics simulation of the cooling chamber of the engine, to provide a calibration and validation of the developed simplified algorithm. The simulation is carried out by setting up a steady-state problem, choice motivated by the fact that the temperature traces collected in the experimental firings reached a plateau roughly five seconds.
Reported below are the procedural steps followed in the analysis:

1. set up a reliable and correct simulation;
2. selection of the best sample case to base one CFD analysis on;
3. iteratively perform a change in the boundary conditions (namely the nozzle temperature) until there is a match in water temperature at the outflow with the experimental data;
4. calibration of the simplified algorithm based on the analysis results;
5. validation through the CFD on some other firings to verify the robustness of the solution.

The first point of the above list is developed in this section. The aim consists in producing a simulation in which results can be trusted. The preliminary step to take is to generate a baseline mesh that accurately describes the heat exchange at hand. To obtain valid results, it is essential to perform a control on the effect of the boundary layer number on the simulation results without decreasing the element size of the polygons used inside the volume. To make more clear what described in the previous sentence it must be said that the number of boundary layers used in a CFD simulation can significantly impact the accuracy of the simulation results, particularly in regions near the walls where the flow behavior changes rapidly. Polygons are instead the geometric shapes that are used to represent the surface and inner volume of the simulation system; for example, regions with high flow velocity gradient or in boundary layers near curved surfaces may require a higher density of polygons for higher accuracy.
The next step is performing a mesh independence study to define the minimum number of mesh elements needed to have good quality output with the least computational burden. The goal of this analysis is to ensure that the results obtained are due to the boundary conditions and physics at play, not the mesh resolution. Figure 14 below is a comparison of three, six, and nine boundary layers in a polygonal mesh of 40,000, 60,000, and 80,000 elements. In all three cases, the cell element size is kept identical, and only the boundary layer count is changed. By increasing the number of boundary layers, the thickness of the cells near the volume boundary is refined, allowing for a better capturing of any strong gradients.
What can be observed is that the difference between three and six boundary layers is significant, while the change between six and nine is negligible. Therefore, to ensure accurate enough calculations near the walls, all meshes from this point forward will have six boundary layers. The mesh independence study shown in Table 2 and Figure 15 is aimed at refining the temperature field inside the fluid domain in order to obtain a mesh capable of giving the most correct results with the use of the least amount of elements possible, to have a lean, but reliable calculation whose result is independent on the mesh used. The study is performed comparing the results of simulations based on the same boundary conditions, but with an increasing number of elements up to one million cells, which is the maximum number allowed in the student version of the ANSYS software. The mesh generation variables used were minimum and maximum element size, as well as maximum cell length. These parameters were selected to generate a mesh that is fine enough to deal with the size of the features of the cooling chamber and nozzle. The parameters were reduced progressively to generate the desired number of cells for the study. In all cases 6 boundary layers and a polygonal mesh type have been used.
The simulations were performed with no boundary conditions on the external surface of the fluid volume thus treated as adiabatic. The inlet temperature is set to 286 K, with a mass flow rate of 0.08 g/s. The water properties were kept constant at a density of 998.2 $\frac{\text{kg}}{\text{m}^3}$, a specific heat of 4182 $\frac{\text{J}}{\text{KgK}}$, a thermal conductivity of 0.6 $\frac{\text{W}}{\text{mK}}$ and a dynamic viscosity of 0.001003 $\frac{\text{Ns}}{\text{m}^2}$. The nozzle is set at 500 K as a preliminary guess generated from the non calibrated MATLAB® code, and the outlet pressure is reasonably set to 1.5 bar. In all cases, the iteration count is stopped at 50 to ensure the same level of convergence between meshes.
What can be deducted from Figure 15 is that up until 100000 elements the simulation does not provide a good representation of the water jet and of the temperature profile inside the chamber, while from 200000 elements upward the result can almost be superposed to the one million cells case. The mesh which gave the best balance between accuracy in terms of temperature profile, water jet shape and output temperature is found at 200000 elements, as reported in Figure 16. The output proved to be closely matched at 300000 elements.

Once the mesh is defined, the subsequent thing to do is setting up the simulation of a sample case. The procedure

consists in guessing the nozzle temperature required to match the outflow water temperature measured by the thermocouple data available after the test. The case chosen for this analysis is a firing involving SEBS20 of the duration of 20 seconds and that presented stable conditions. This makes it suitable for the calibration, since the CFD is based on steady-state. All the boundary conditions are the same used for the mesh-refining, except for the temperature of the nozzle, which is varied iteratively until the water temperature at the outlet is matched with the experimental data. The number of iteration needed to reach a satisfying convergence of the results is 400 iterations.

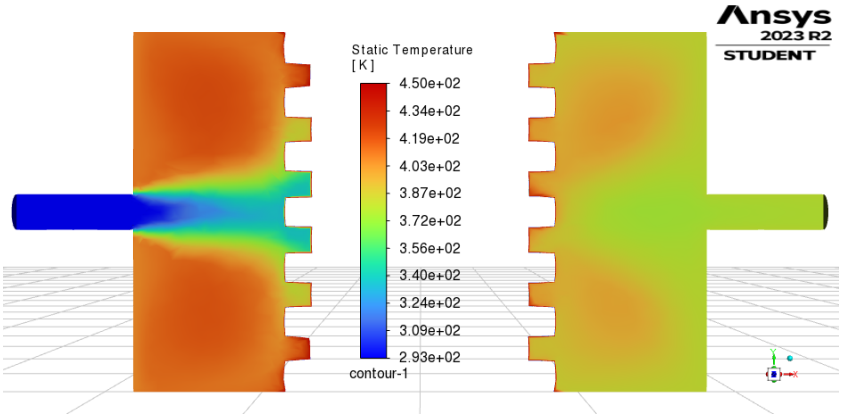

(a)

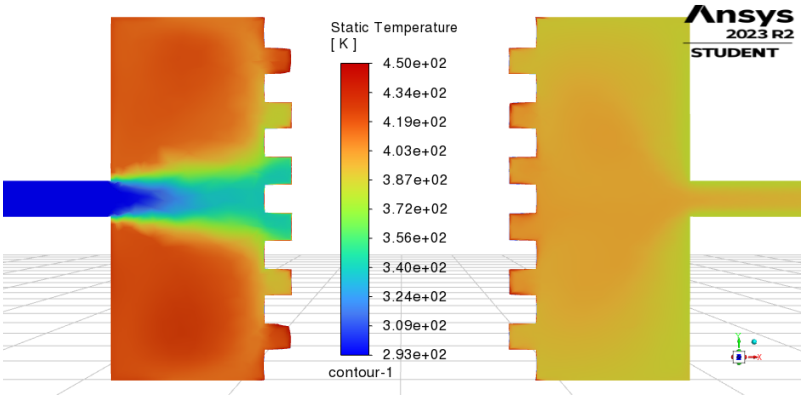

(b)

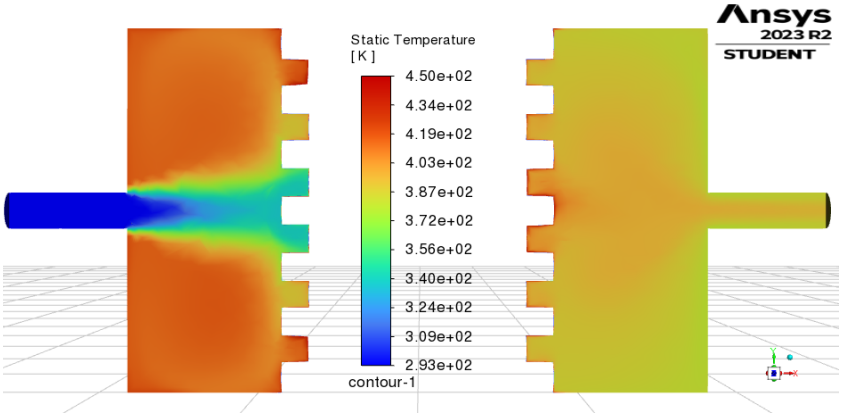

(c)

Figure 14: Boundary Layer number variation: (a) 3 BL Polygonal, (b) 6 BL Polygonal and (c) 9 BL Polygonal.

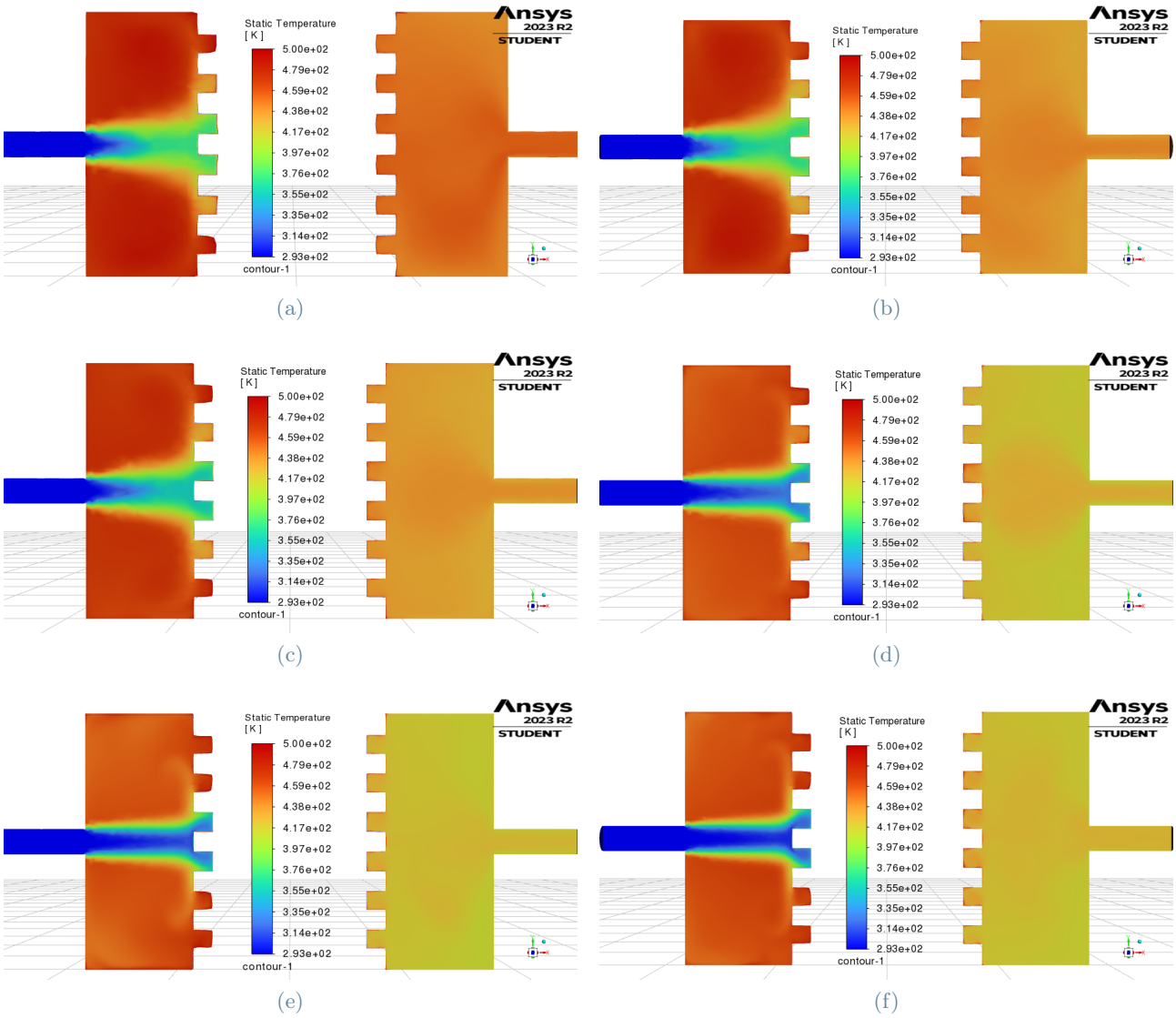

Figure 15: Mesh independence study: (a) 36k elements, (b) 63k elements, (c) 100k elements, (d) 200k elements, (e) 300k elements and (f) 1M elements.

Table 2: Variables of interest in the meshing process.

Min el. size [mm]	**Max el. size** [mm]	**Max cell length** [mm]	# **cells** [-]
1	3	4.45	36000
1	2	2.67	63000
0.75	1.5	1.85	100000
0.25	1.2	1.25	200000
0.1	1	1	300000
0.01	0.5	0.85	1000000

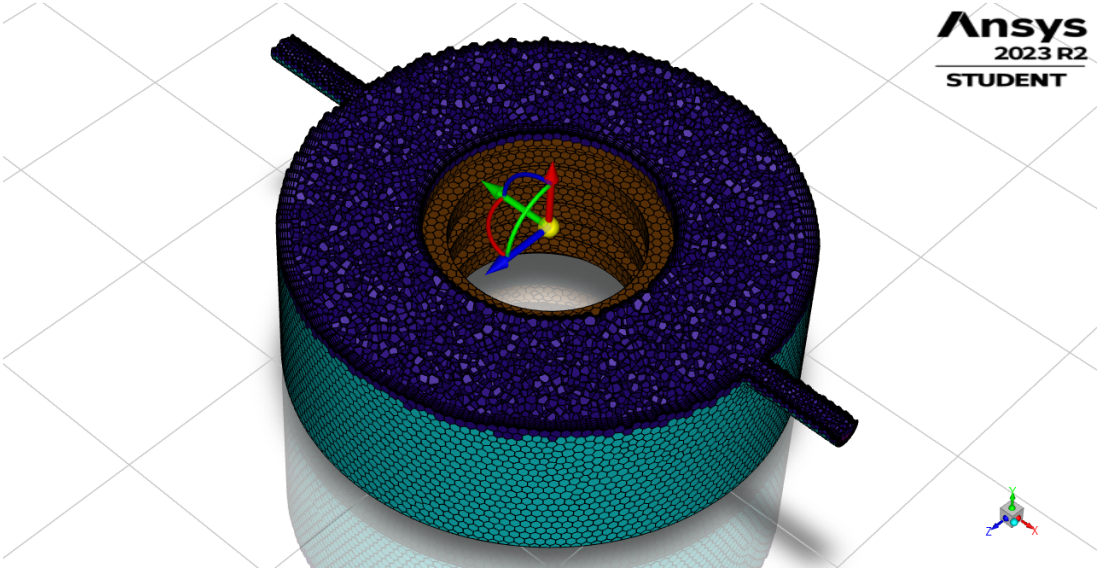

Figure 16: 200000 elements mesh selected for the simulation.

7.4. Algorithm tuning and accuracy

The results of the CFD validation is a detailed simulation involving temperature and fluid behaviour based on the SEBS20 reference firing: It allowed the definition of the α parameter introduced in Eq. (17), together with the velocity of the water jet to be used in the definition of the numbers requiring it. A qualitative analysis of the simulation output in Figure 17, which is a vertical cross section of the combustion chamber, revealed that a quarter of the cylinder is invested by a flow significantly faster than in the rest of the chamber. Therefore the cylinder in cross flow model is used in the region with faster water velocity and the free convection model where it is slower. The results also allow to calculate, by performing an average of velocity values on the aperture of the jet just before the impingement point and to treat this value as an asymptotic velocity investing the cylinder. Referring to Figure 17 reported below, a value of 3.8 m/s is the one calculated for the jet velocity and the alpha coefficient is set as $\alpha = 0.25$.

$$\dot{m}_w c_{p,w}(T_{w,out} - T_{w,in}) = h_{wn,real} A_n (T_n - T_{wv}) = \lambda \left(\frac{3}{4} h_{Free} + \frac{1}{4} h_{Forced} \right) A_n (T_n - T_{wv}) \tag{21}$$

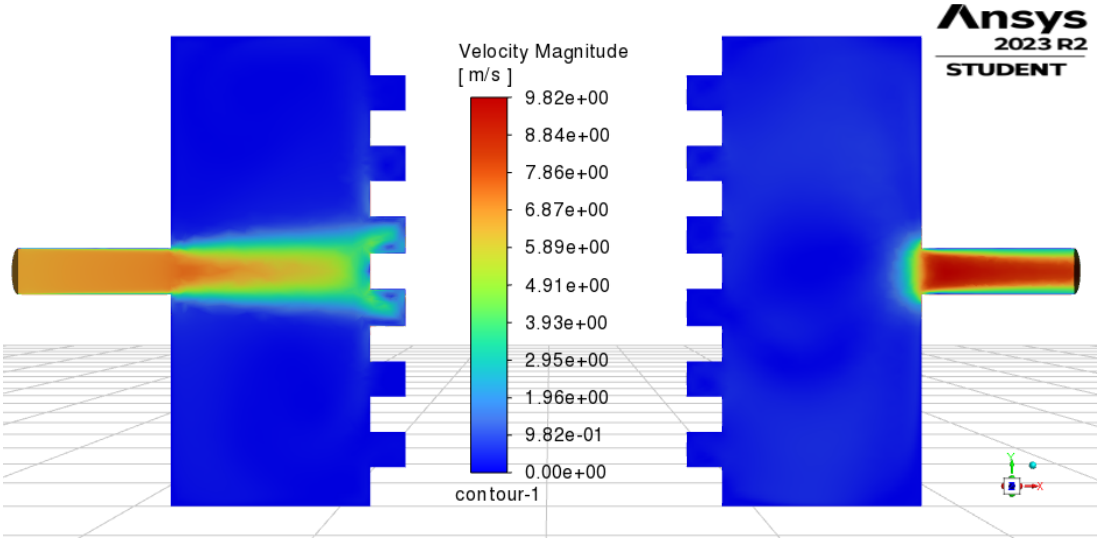

Figure 17: Vertical plane section view of the nozzle cooling chamber water velocity.

This reduces the unknown parameters to only one, λ, the corrective multiplier for the convective heat transfer coefficients presented in Eq. (21).
The complete thermal fluid dynamics simulation performed is used to tune this last parameter in order to obtain

in the code the same nozzle surface temperature as the one set in the CFD analysis to obtain the match in the outflow water temperature of the SEBS20 firing used as reference.
The calibration results in a λ coefficient of 2.23. After that, what follows is a verification of the code robustness using other firing data. The aim of this step is to assess the predictive capability of the MATLAB® code for conditions outside of the sample case. The tests chosen are run on the code and then simulated in ANSYS with the same exact settings and iterations. Between cases, the input regarding the inlet water temperature provided by the thermocouple and the nozzle temperature returned by MATLAB® were the only ones changed. Table 3 below sums up the results of the verification procedure in decreasing nozzle temperature order. Columns represent in the order reported: the water temperature at the inlet as measured by the thermocouple, the temperature of the nozzle calculated by the MATLAB® code, the temperature measured bu the thermocouple at the exit from the cooling chamber, the temperature at the outlet simulated by ANSYS and finally the relative errors between simulated and measured temperature.
What can be deduct from these results is a globally good prediction of the results. Eq. (22) and (23) are used to calculate the relative errors expressed in Table 3 in percentage form:

$$\epsilon_{wv,rel} = T^{AN}_{w,out} - T^{tc}_{w,out} \tag{22}$$

$$\epsilon_{wv,rel,\%} = \frac{T^{AN}_{w,out} - T^{tc}_{w,out}}{T^{tc}_{w,out} - T^{tc}_{w,in}} \cdot 100 \tag{23}$$

At the numerator of Eq. (23) compares the absolute difference between the ANSYS simulation and the thermocouple data, while at the denominator there is the difference measured by the instrument between inlet and outlet conditions. The errors calculated for the two most extreme conditions representing the lowest and highest nozzle temperature of the cases reported were found to be fairly comparable, demonstrating an overall consistency of the code downwards and upwards of the SEBS20 firing test chosen for the calibration.

Table 3: Calibration and verification firings.

Case ID	$\mathbf{T^{tc}_{w,in}}$ [K]	$\mathbf{T^{MA}_{n}}$ [K]	$\mathbf{T^{tc}_{w,out}}$ [K]	$\mathbf{T^{AN}_{w,out}}$ [K]	$\mathbf{\epsilon_{wv,rel}}$ [K]	$\mathbf{\epsilon_{wv,rel,\%}}$ [-]
SEBS20_R2b	**293.6**	**470**	**326**	**326**	**0**	**0**
SEBS20_R3a	287.5	553	341.8	333.8	-8	-14.73
SEBS5_R4	288.9	504.5	330.5	326.5	-4	-9.62
ABS_R2b	297.3	425	320	319.6	-0.4	-1.76
SEBS10_R4	291.5	412	312	312.5	+0.5	+2.44
ABS_R4	287.8	376	301.5	303.2	+1.7	+12.41

The SEBS5 case reported in Table 3 represents a firing not long enough to reach a steady state condition, which might translate in an increased error in the predictive capability of the code, which assumes steady state conditions. While this might still be, by applying the same formula reported above what is found is a 10% error, which falls within the maximum error calculated before, conforming that the code can be used to retrieve reliable data even for tests which fall within the predicted nozzle temperature window. The firing is included anyways to give an idea of the predictive capability in situations far from the steady state.

8. Firing test campaign

The experimental test campaign is performed on the VFP engine presented in Chapter 2. Tested fuels are listed in Chapter 3 in Table 1; they are ABS and different blends of paraffin. These fuels were tested in combination of oxygen as oxidizer, at different levels of mass flow rates to span multiple O/F and total mass flux testing

conditions. The theoretical burning time is adapted during the different tests in order to not stress the engine and save some residual fuel mass for the post processing and as function of the mechanical properties as well (faster fuels fire for shorter times). Also, the general rule of thumb followed consists in decreasing the burning time when the oxidizer mass flow rate is higher in order to have balanced grain consumption. The experimental matrix is hereby reported, in Table 4.

Table 4: Experimental matrix of the performed tests: number of firings is reported, as function of the fuel type and oxidizer mass flow rate. One SEBS20 firing is marked * because a different nozzle was used (brass, $\varepsilon = 4$).

	4g/s	6g/s	7g/s	7.5g/s	8g/s	8.5g/s	9g/s	10.5g/s	11g/s	12g/s	13g/s
ABS	2	3	-	-	2	-	1	-	-	-	-
SEBS5	-	-	1	-	-	-	-	-	2	-	2
SEBS10	-	2	-	2	-	-	1	-	-	-	-
SEBS20	-	2	2	-	-	-	2	1	1*	1	-
W1	-	1	-	-	-	-	-	-	-	-	-

The ballistic performances of interest retrieved from the tests are the regression rate function of the total mass flux and combustion efficiency in terms of characteristic velocity. The regression rate is computed via a "thickness over time" (TOT) approach based on the measurement of the grain weights before and after the firing. Since the engine configuration presents two fuel disks regressing at the same time, the regression rate is calculated for both and a final average value is provided as well. A single disk regression rate is computed as:

$$r^i_{f,avg} = \frac{\Delta m^i_{grain}}{\rho_f A_f \Delta t_b} \tag{24}$$

where the apex i can be used to define the NO or N2 side disk, where the first is the nozzle facing one and the second is the opposed one. Δm^i_{grain} is the mass difference of a given disk before and after the combustion, ρ_f is the theoretical fuel density, Δt_b is the burning time as reported in Chapter 6 and A_f is the burning surface of the fuel disk and is calculated as: $A_f = 0.25\pi(D_f^2 - D_i^2)$, with $D_f = 86$ mm is the external diameter of the fuel grain and $D_i = 25mm$ is the diameter of central perforation that fits the carbon tube.

The computation of the regression rate is therefore calculated as the mean of the two fuel grains and is expressed in mm/s.
The computation of the total mass flux is instead based on the amount of gas traversing a radial section of the combustion chamber spanning its variable height over time and its fixed width, determined by the central symmetry axis and the internal wall of the injection ring. The height of the combustion chamber, function of time, can be linearized as:

$$h_{cc}(t) = h_{cc,0} + 2 \cdot r_{f,avg}\, t \tag{25}$$

where $2 \cdot r_{f,avg}$ is due to both disks regressing simultaneously and $h_{cc,0}$ is fixed at 20 mm. From the previous equation is possible to compute the final combustion chamber height by substituting the burning time.
By substitution of Eq. (24) and burning time t_b into Eq. (25) the following final chamber height is retrieved:

$$h_{cc,f} = h_{cc,0} + 2 \cdot \frac{\Delta m_{tot}}{\rho_f A_f} \tag{26}$$

where Δm_{tot} is the total mass burnt during the burning window.
For the calculation of the average total mass flux, an average algebraic chamber height is used:

$$h_{cc,avg} = 0.5 \cdot (h_{cc,0} + h_{cc,f}) \tag{27}$$

providing the following average expression:

$$G_{tot,avg} = \frac{\dot{m}_{f,avg} + \dot{m}_{ox,avg}}{0.5\ D_f\ h_{cc,avg}} \tag{28}$$

where $\dot{m}_{ox,avg}$ comes from Eq. (5). The average fuel mass flow rate is computed as:

$$\dot{m}_{f,avg} = r_{f,avg} \frac{A_f}{\rho_f} \tag{29}$$

The efficiency of the combustion chamber is commonly expressed in terms of the c^* parameter, which is defined as the product of chamber pressure p_{cc} and throat section A_t divided by the total mass flow rate $\dot{m}_t$ traversing that section.

$$c^*_{real} = \frac{p_{cc} A_t}{\dot{m}_t} \tag{30}$$

An efficiency parameter can be defined from the comparison of the above defined c^* with an ideal one. This latter can be computed with the use of Chemical Equilibrium with Applications (NASA-CEA) code, that requires as input the chamber pressure and O/F ratio, along with information (chemical formula, enthalpy of formation, storage temperature) about oxidizer and fuel.

$$\eta_{c^*} = \frac{c^*_{real}}{c^*_{CEA}} \tag{31}$$

9. Results

In this chapter the collection of data of the experimental firing campaign along with noteworthy results are presented. A first section is dedicated to the presentation of the data collected from the experimental campaign and the ones obtained from MATLAB® regarding all the 28 firings performed; a second section will then be dedicated to the presentation of the ballistic data of interest of all the firings, along with a table containing the regression rates as a function of the total mass flux, where to the 28 firings contained in the tables, some additional ones are added in order to perform a better interpolation.

9.1. Heat transfer results

The tuned algorithm after the CFD, allowed to have a faster way to compute the quantities of interest of the rest of the firings that have not been employed in the calibration. The copper nozzle has a volume of material of 29 cm^3, a surface area of 56 cm^2 inclusive of the 5 fins surface, a density of 8.933 g/cm^3, a throat area of 5 mm and an expansion ratio of 2. The aluminium case has a volume of 96.6 cm^3 and is fed at a rate of 80 ml of water every second. The final parameters used in the code regarding the water velocity for the cylinder in cross flow, the fraction of chamber assigned to each of the two heat transfer models discussed in Chapter 7 and the corrective parameter found as a result of the CFD analysis are respectively: 3.8 m/s for the water velocity, $1/4 = \alpha$ and $3/4 = (1 - \alpha)$ for the cylinder in cross flow and natural convection models and $\lambda = 2.23$ for the corrective parameter for the tuning of the heat transfer coefficient. Figure 18 is an example of computed temperature traces relative to the calibration test SEBS20_R2b. A consideration on its focus around ignition time, Figure 19, regards the nozzle temperature. Another finite impulse response filter is used on it, as the one in Chapter 6, this time with a filter order of 10^3 and a cutoff frequency of 1 Hz, in order to smooth the trace to remove non-physical discontinuities.

Table 5 sums up the experimental campaign performed. Some considerations on the results can be made:

- the nozzle temperature spans from 376 K obtained in one of the ABS firings to 553.2 K in the most demanding case of SEBS20, non resulting in any damage to the setup;
- the peak heat subtracted from the gas is 13.7 kW;
- the first SEBS20 firing reported in Table 5 is relative to the only firing test where a brass nozzle different from the copper one is used, with the same throat diameter of 5 mm and an expansion ratio of 4 instead of 2. Because of the lower thermal conductivity of brass compared to the one of copper, the firing may have caused the nozzle to overheat and lose some of its mechanical properties that caused it to fail to withstand the shear forces generated by the gas and ended up with a meltdown.

Some considerations on the power leaving the gas can be made starting from the data presented in Table 5. As can be seen, the power stored inside the nozzle and therefore contributing to the heating of the bulk material ranges from roughly 10% in longer firings, such as SEBS20_R2b to over 40% in shorter firings, such

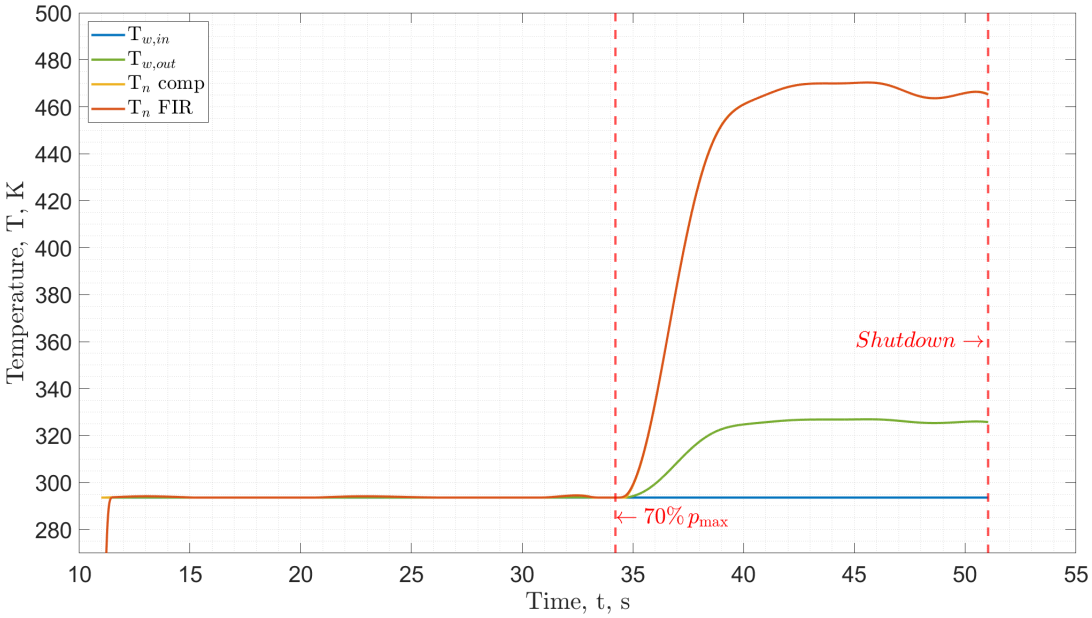

Figure 18: Temperature traces of water and nozzle.

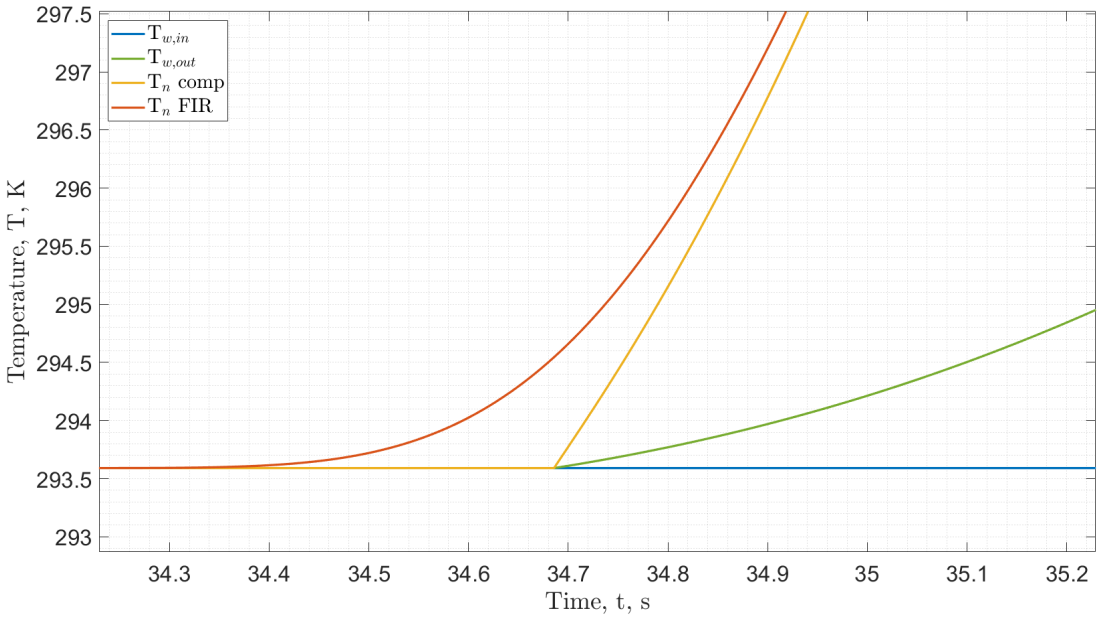

Figure 19: FIR filter smoothing the calculated temperature of the nozzle.

as SEBS20_R4a, where the firing duration is as long as the typical duration of the transient.
These data fall in line with the evaluation performed in Reference [13] by Haag, where a peak power advected by the water of 7.3 kW corresponding to 18% of the total power of the gas is found. In his analysis all the considerations were performed on one second windows of data where the engine is assumed in steady state condition and therefore not including transient conditions as in this study; losses are evaluated as water heat and as Eq. (9); the total exhaust power, representing the total one is calculated with the following formula:

$$\dot{Q}_g = \frac{T\, v_e}{2} \tag{32}$$

where T is the thrust measured by the load cell and v_e is the exhaust gas velocity at the exit of the nozzle.

Figure 20 represents the heat power absorbed by the water, the one of the nozzle and the one of the gas. The first is always positive as the water is always heated by the nozzle, the second has a first positive peak, but then

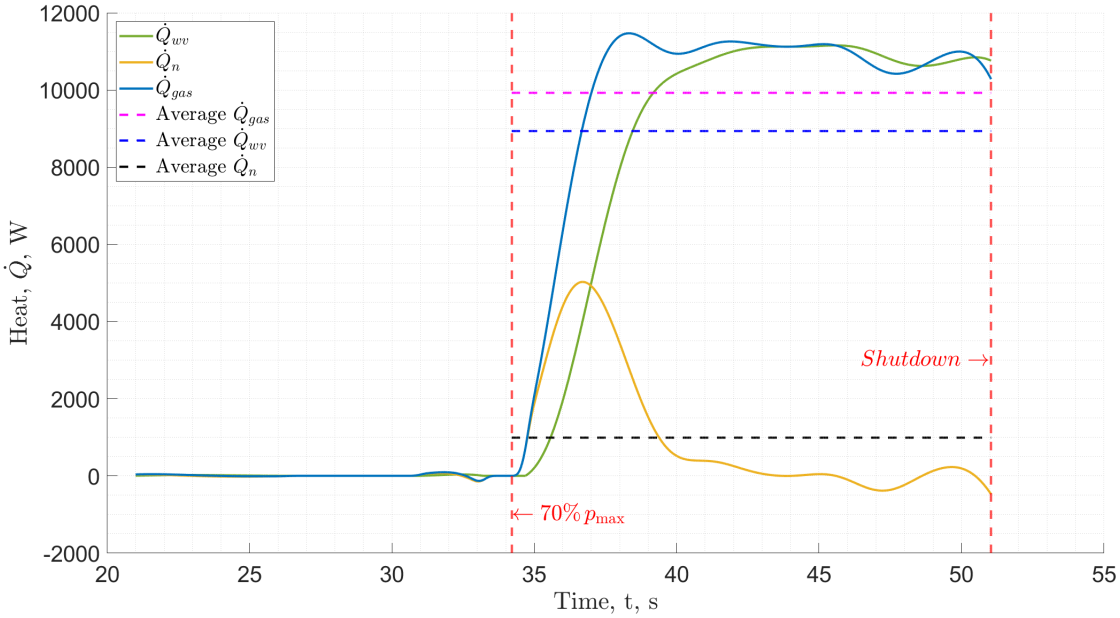

Figure 20: Heat flux magnitude and direction.

decreases to zero when steady state conditions are reached.
Up to this point, the assumption of considering a uniform temperature inside the nozzle and treating the problem as a steady-state, has allowed us to simplify the problem considerably. It is now possible to make some further considerations on the validity of that simplification. An important observation regarding the Biot number must be made. It is a dimensionless parameter that provides a measure of the temperature drop inside of the material when its exchanging heat with a fluid, in this case water.

$$Bi = \frac{R_{cond}}{R_{conv}} = \frac{h_{wn} D}{k_c} \tag{33}$$

where R_{cond} is the conductive heat transfer resistance, R_{conv} is the convective heat transfer resistance, h_{wn} is the convective coefficient, D is the characteristic dimension and k_c is the copper thermal conductivity.
The Biot number can be interpreted as the ratio of conductive resistance to convective resistance. In particular, from the definition of Eq. (33) it is evident that if $Bi \leq 1$, the resistance to conduction within the solid is much less than the resistance to convection across the fluid boundary layer. Hence, the assumption of a uniform temperature distribution within the solid is reasonable if the Biot number is small. indicatively if $Bi \leq 0.05-0.1$ the error may be lower than 5%.
In this work, values of the Biot number obtained range between 0.1 and 0.2. Therefore, temperature gradients in the radial direction should be considered in a more precise transient analysis model to minimize errors. Furthermore, in the nozzle there are temperature gradients in the axial direction due to the significant temperature variation that the exhaust gases face during the expansion process. These have been ignored. The same consideration can be made for the surface facing the cooling chamber, which will exhibit temperature gradients due to the difference in convective dissipation between the portion of the nozzle impacted by the water jet and the portion considered under free convection. Therefore, considering the nozzle at uniform temperature even though is subject to significantly different boundary conditions is the biggest approximation of the proposed model. Although having non negligible errors on the heat accumulated inside nozzle, it is important to underline that those errors are reduced due to the 10%-40% of nozzle heat influence on the total, thus it is correct to assume the single-node hypothesis as a good approximation for the objectives of the model.

Table 5: Maximum temperatures and average heat powers output of the thermal model for the performed firing tests.

Case ID	$T_{w,in}[K]$	$T_{w,out}[K]$	$T_n[K]$	$\overline{\dot{Q}}_{wv}[kW]$	$\overline{\dot{Q}}_n[kW]$	$\overline{\dot{Q}}_g[kW]$
ABS_R0	-	-	-	-	-	-
ABS_R1a	-	-	-	-	-	-
ABS_R2a	286.0	307.3	415.0	5.01	1.11	6.12
ABS_R3a	286.0	302.0	389.5	4.17	0.630	4.80
ABS_R4	287.8	301.5	376.0	3.54	0.58	4.12
ABS_R1b	297.0	320.3	426.3	5.26	1.09	6.36
ABS_R2b	297.3	320.3	425.5	5.37	1.12	6.49
ABS_R3b	298.3	320.0	419.5	4.75	1.19	5.94
SEBS5_R1a	286.9	317.3	458.2	7.16	2.00	9.17
SEBS5_R2	285.7	314.0	448.2	6.68	1.93	8.61
SEBS5_R3	286.6	322.7	482.5	8.00	2.36	10.35
SEBS5_R4	289.0	330.5	504.6	9.11	2.67	11.78
SEBS5_R1b	293.0	327.5	475.6	7.92	1.36	9.28
SEBS10_R1	294.4	311.5	396.0	4.18	0.61	4.80
SEBS10_R2	295.3	310.2	385.6	3.77	0.55	4.34
SEBS10_R3	291.5	312.0	412.3	4.80	1.00	5.80
SEBS10_R4	291.4	311.3	409.2	4.47	1.13	5.60
SEBS10_R5	292.4	315.5	424.6	5.43	1.21	6.64

Case ID	$T_{w,in}[K]$	$T_{w,out}[K]$	$T_n[K]$	$\overline{\dot{Q}}_{wv}[kW]$	$\overline{\dot{Q}}_n[kW]$	$\overline{\dot{Q}}_g[kW]$
SEBS20_R2a*	289.3	329.2	498.0	7.78	2.02	9.80
SEBS20_R3a	287.5	341.8	553.2	11.68	1.99	13.67
SEBS20_R4a	292.5	337.4	516.2	6.69	4.87	11.56
SEBS20_R2b	293.6	326.0	470.0	8.93	0.99	9.93
SEBS20_R2c	292.0	328.2	482.4	8.43	1.26	9.69
SEBS20_R3b	294.5	312.0	398.5	4.59	0.65	5.24
SEBS20_R4b	295.5	314.3	405.2	4.85	0.68	5.53
SEBS20_R5	297.7	321.2	427.5	5.60	1.23	6.84
SEBS20_R6	297.6	321.4	429.2	5.45	1.31	6.76
W1_R1	292.3	306.5	381.0	3.58	0.44	4.02

9.2. Ballistic analysis

This section will discuss the ballistic data collected and calculated from the firing tests, which have a theoretical burning time of seven to twenty seconds, a fixed initial combustion chamber height, which is the same in all the tests and a variable oxidizer mass flux, whose increase affects positively the regression rate. The experimental campaign results revealed a non-negligible loss of mass in the nozzle-facing carbon tube, which led to efficiencies that often exceeded unity. This is not a physical result and, therefore, it is decided to implement a modification to the formulation of the characteristic velocity, reported in Eq. (34), due to the unexpected loss in mass of the nozzle side (NO) carbon tube that is found to be between 10 and 25 percent of the total mass lost in the firings. As a result, the lost mass is incorporated into the total mass flux of the gas flow that expands in the convergent-divergent nozzle. This modification led to the formula evaluating the empirically determined c^* incorporating a quantity of mass flow rate linked to the carbon tube burning in the denominator. Adding this term to the formula (30) results in:

$$c^*_{real} = \frac{p_{cc}A_t}{\dot{m}_t} = \frac{p_{cc}A_t}{\dot{m}_{ox} + \dot{m}_f + \dot{m}_{CT}} \tag{34}$$

where $\dot{m}_t$ is the total mass flow rate, which can be expressed in its constituents, namely: $\dot{m}_{ox}$, $\dot{m}_f$ and $\dot{m}_{CT}$ are respectively the oxygen, the fuel and the carbon tube mass flow rate.
This term related to carbon tube is not considered in the $G_{tot,avg}$ Eq. (28): since only the carbon tube on the nozzle side erodes, its contribution is found only within the nozzle that lies below it. It is reasonable assuming that its mass does not circulate in the combustion chamber and does not contribute to the total mass flux.
The data are processed using the formulas illustrated in Chapter 8. The main input variables and the obtained results are collected in Table 6. Regarding the regression rate, the results obtained through the Eq. (24) are fitted using the power law:

$$r_f = a_r \cdot G_{tot}^{n_r} \tag{35}$$

where a_r and n_r are the proportional and exponential coefficients and they are compared and collected in Table 7 while G_{tot} is the total mass flux. Figure 21 allows a visual comparison of the regression rate as function of the total mass flux for all the tested fuel formulations.

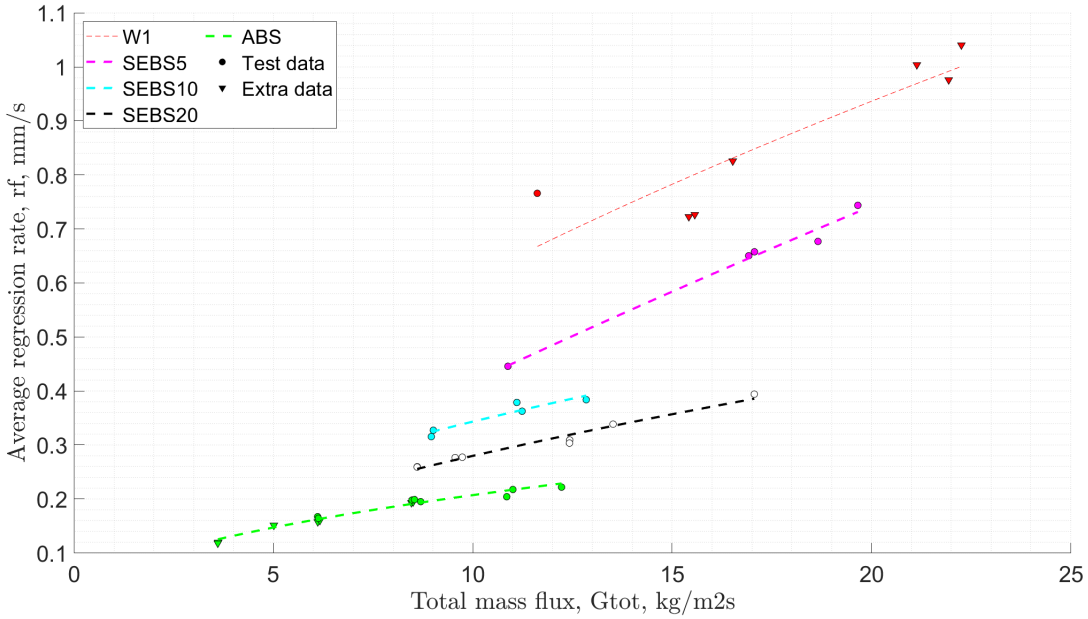

Figure 21: Regression rate plot as function of the total mass flux for the investigated fuel formulations.

In Figure 21, the represented data have been processed through the regression rate power law of Eq. (35). For completeness, in addition to the data obtained during this work, previously acquired data from the laboratory have been utilized, referred to as *Extra data*. In particular, the additional values correspond to the firings of ABS and W1. Those data are taken from [28].
From the data related to the regression rate and from the Figure 21, it is observed that ABS is characterized by lower performance, with an exponential coefficient n_r=0.4134. SEBS10 and SEBS20 exhibit a n_r similar to ABS (respectively, 0.5371 and 0.5803). This is due to the high percentage of thermoplastic contained in these paraffin-based fuels. Regarding SEBS5, and W1 after that, the regression rate is higher compared to the other fuels. Its high exponential factor suggests an enhanced regression rate due to the entrainment phenomenon of the melt layer, as discussed in Ref. [16] and [17]. Indeed, regression rate shows a behaviour opposite to mechanical properties.

As regards combustion efficiencies, minimum value is $\sim$ 80% and they reach value up to 99.9%. One case exceed 100% but it coincides with the same firing with nozzle loss, thus it is reasonable to have a non-sense value.

Table 6: Input variables, chamber pressure, thrust, total mass flux, regression rate and efficiencies for the performed firing tests.

Case ID	$\dot{m}_{ox}$ [g/s]	Δt_b [s]	P_{avg} [MPa]	T_{avg} [N]	$G_{tot,avg}$ [kg/m^2s]	$r_{f,avg}$ [mm/s]	$\eta_{c^*,\%}$ [-]
ABS_R0	5.98	14.18	0.60	14.59	8.48	0.20	86.0
ABS_R1a	5.98	13.33	0.62	15.75	8.54	0.20	88.7
ABS_R2a	6.02	10.93	0.62	16.17	8.69	0.20	89.3
ABS_R3a	3.99	15.50	0.41	10.22	6.11	0.17	79.3
ABS_R4	3.99	14.26	0.41	10.23	6.13	0.16	81.2
ABS_R1b	8.02	11.30	7.47	18.78	10.85	0.20	84.6
ABS_R2b	9.06	9.69	8.31	21.15	12.23	0.22	84.3
ABS_R3b	8.04	10.84	7.69	18.96	11.00	0.22	85.0
SEBS5_R1a	11.13	7.67	1.53	37.35	17.06	0.66	97.2
SEBS5_R2	11.08	7.78	1.54	39.22	16.92	0.65	98.6
SEBS5_R3	12.79	7.99	1.76	43.10	18.66	0.68	99.1
SEBS5_R4	13.32	7.71	1.80	43.93	19.66	0.74	96.0
SEBS5_R1b	7.02	12.83	0.85	20.86	10.88	0.45	83.0
SEBS10_R1	6.03	14.63	0.73	17.34	8.96	0.32	83.2
SEBS10_R2	6.02	14.72	0.72	17.31	9.01	0.33	82.3
SEBS10_R3	7.51	11.45	0.90	22.46	11.10	0.38	83.7
SEBS10_R4	7.56	9.92	0.89	21.53	11.24	0.36	84.0
SEBS10_R5	9.08	10.29	1.07	27.32	12.84	0.38	87.5

Case ID	$\dot{m}_{ox}$ [g/s]	Δt_b [s]	P_{avg} [MPa]	T_{avg} [N]	$G_{tot,avg}$ [kg/m^2s]	$r_{f,avg}$ [mm/s]	η_{c^*},% [-]
SEBS20_R2a*	287.5	10.09	1.78	35.69	14.82	0.40	125.1
SEBS20_R3a	10.92	13.21	1.28	32.33	13.52	0.34	99.9
SEBS20_R4a	10.41	4.37	1.46	37.76	17.06	0.39	97.4
SEBS20_R2b	7.04	16.84	0.81	20.36	9.56	0.28	86.7
SEBS20_R2c	7.06	14.77	0.82	19.70	9.74	0.28	92.7
SEBS20_R3b	6.06	15.12	0.68	16.98	8.60	0.28	81.7
SEBS20_R4b	6.04	14.93	0.67	16.47	8.60	0.26	81.8
SEBS20_R5	9.09	10.12	0.99	25.16	12.43	0.31	86.9
SEBS20_R6	9.07	9.65	0.97	25.07	12.42	0.30	86.0
W1_R1	6.04	14.97	0.73	18.56	11.62	0.77	82.0

Table 7: Regression law coefficients, coefficient of determination, standard deviation and total mass flux tested range of validity for the investigated fuel formulations.

Fuel	$a_r[\frac{mm/s}{(kg/m^2s)^{n_r}}]$	$n_r[-]$	R^2[-]	G_{tot} validity range [kg/m^2s]
ABS	0.0633	0.5179	0.9664	$3.59 < G_{tot} < 12.23$
SEBS5	0.0609	0.8347	0.9844	$10.88 < G_{tot} < 19.66$
SEBS10	0.0995	0.5371	0.8930	$8.96 < G_{tot} < 12.84$
SEBS20	0.0738	0.5803	0.9683	$8.60 < G_{tot} < 17.06$
W1	0.1709	0.5648	0.7868	$11.62 < G_{tot} < 22.25$

10. Conclusions

The research investigates the development of a heat transfer model capable of describing the heat losses in the exhaust gas of a vortex flow Pancake hybrid rocket motor, a novel configuration with promising capabilities for future space propulsion applications. The heat losses are caused by the introduction of a water cooling system for the nozzle which aims at prolonging its life cycle and avoiding the meltdown during operation and by the heat captured and stored inside the nozzle bulk, made of copper. The first steps of this analysis aimed at modeling the heat transfer problem happening inside the cooling chamber enclosing the nozzle with empirical formulations for cylinders in cross flow and natural convection implementations. The data and variables needed to model the problem and make the numerical formulation work are collected via experimental tests of sort and a firing campaign of the engine. Thus, an algorithm embedding the theoretical transient model was designed with the objective of a fast-accurate post-processing of the firing tests. The validation of the results obtained with the code have been performed through a CFD analysis of the heat convection problem, which started with the generation of an optimal mesh that produced a good description of the geometry and accurate results without being overly refined in the elements used, to allow for reasonably quick simulations. By utilizing the data collected in the runs of the engine as boundary values for the simulation, and by selecting the best sample cases, is possible to calibrate the code and refine the heat transfer problem to allow for good predictive capability and accordance between the two. What this CFD analysis has allowed to do is to obtain a code capable of providing the heat subtracted from the gas for a wide range of working conditions. The experimental campaign concerning the firings is organized with the logic of performing tests spanning a wide range of conditions and multiple tests were performed for every case in order to exclude errors deriving from anomalies. A well structured test campaign allowed to generate the regression laws correspondent to every fuel tested and to collect all the data needed to calculate the heat losses.
Results demonstrated that the cooling system is well-designed and maximum predicted nozzle temperatures do not exceed 555 K. Temperature is function of the tested fuel formulation as well of the gas mass flow rate in the nozzle. The results obtained in terms of power subtracted from the gas for the transient case modeled span from 4 to over 13 kW, in accordance with the literature. The produced model is generally accurate, but the hypothesis behind the heat power associated to the nozzle are strong and errors might not be negligible. However, their effect on the final result of the heat loss by the gasses is damped by the biggest contribute coming from water cooling heat transfer, which is from 60 to 90% of the total for the tested conditions. Errors drops with longer firing; for more than 20 seconds, a steady state approximation can be considered.
Ballistic analysis allowed to compute regression rate laws for different fuel formulations at different mass flow rates. ABS and different paraffin blends were tested. The outcome is a regression rate higher for fuels tending to pure paraffin, thus lower mechanical properties. The entrainment effect to which paraffin-based fuels are subjected is the reason of their high regression rate.

Abstract in Italiano:

Un motore a razzo ibrido è un sistema di propulsione termochimica che utilizza combustibile e ossidante in due diversi stati di aggregazione. Questi motori presentano diversi vantaggi come flessibilità operativa, se comparata a motori a propellenti solidi, semplicità dell'architettura, se confrontata a quella di tradizionali motori apropellente liquido, nonché costi ridotti dovuti sia alla ridotta complessità e al prezzo dei combustibili. Tuttavia, le formulazioni tradizionali del grano solido impiegate mostrano basse velocità di regressione e il propellente richiede più tempo per una corretta miscelazione. Ciò comporta che i motori abbiano un alto rapporto lunghezza-diametro (L/D) o geometrie di grano più complesse per aumentare la spinta, portando a problemi strutturali e riducendo le efficienze volumetriche. Inoltre, la fiamma diffusiva nei motori ibridi porta a efficienze di combustione relativamente inferiori rispetto ad altri sistemi di combustione termochimica. Queste limitazioni hanno ostacolato l'applicazione dei sistemi di propulsione a razzo ibridi sia nei lanciatori che nella propulsione spaziale.
Il Vortex Flow Pancake (VFP) rappresenta una configurazione non convenzionale per un motore ibrido. In particolare l'iniezione tangenziale di ossidante genera un campo di flusso vorticoso nella camera di combustione, individuata dallo spazio tra due dischi di combustibile solido. Lo spazio tra i due dischi è più piccolo del loro diametro, risultando in un motore compatto caratterizzato da un rapporto $L/D < 1$. Il flusso vorticoso porta a una migliore miscelazione del propellente, migliorando dunque l'efficienza di combustione, inoltre fornisce protezione termica alle pareti laterali della camera di combustione grazie al flusso di ossidante. Inoltre, questo design innovativo riduce drasticamente il fenomeno di variazione del rapporto ossidante/combustibile (O/F) durante la combustione, un inconveniente comunemente osservato negli HRE tradizionali. Questa ricerca si propone di modellare un problema di trasferimento di calore per valutare la potenza sottratta ai gas di scarico in espansione da un ugello raffreddato ad acqua di un motore VFP sviluppato presso il Politecnico di Milano (SVFP). La prima parte di questo lavoro coinvolge lo studio di un modello termico per descrivere il problema attraverso correlazioni empiriche provenienti dalla letteratura. Una volta descritto il problema, è stato utilizzato un codice per analizzare i dati di temperatura ottenuti tramite una campagna di test sperimentali. Infine, un'analisi CFD è stata impiegata per tarare questo codice e renderlo accurato. I risultati hanno dimostrato la funzionalità del codice fornendo una stima delle temperature raggiunte dall'ugello e della potenza termica estratta dalla camera di raffreddamento ai gas di scarico. Inoltre, è stata condotta un'analisi balistica utilizzando dati provenienti dai test per diverse formulazioni di carburante.

References

[1] Prusa. https://www.prusa3d.com/.

[2] Prusa website, ABS filament. https://shop.prusa3d.com/en/filament/134-orange-easyabs-filament-1kg.html.

[3] Sasol. https://www.sasol.com/.

[4] Sasol paraffin wax SasolWax 0907. https://www.sasol.com/sasolwax-0907.

[5] Sigma-aldrich. https://www.sigmaaldrich.com/IT/it.

[6] Sigma-Aldrich Carbon Powder. https://www.sigmaaldrich.com/IT/it/product/aldrich/282863?context=product.

[7] Sigma-Aldrich SEBS-MA. https://www.sigmaaldrich.com/IT/it/product/aldrich/432431?context=product.

[8] Theodore L Bergman. *Fundamentals of heat and mass transfer*. John Wiley & Sons, 2011.

[9] Riccardo Bisin, Christian Paravan, Sebastiano Alberti, and Luciano Galfetti. A new strategy for the reinforcement of paraffin-based fuels based on cellular structures: The armored grain—mechanical characterization. *Acta Astronautica*, 176:494–509, 2020.

[10] Riccardo Bisin, Alberto Verga, Daniele Bruschi, and Christian Paravan. Strategies for paraffin-based fuels reinforcement: 3d printing and blending with polymers. In *AIAA Propulsion and Energy 2021 Forum*, page 3502, 2021.

[11] Dave M Gibbon and Gary S Haag. Investigation of an alternative geometry hybrid rocket for small spacecraft orbit transfer. *SURREY SATELLITE TECHNOLOGY LTD GUILDFORD (UNITED KINGDOM)*, 2001.

[12] Mattia Gorini and ALESSANDRO GHIDOTTI. Toward high performance paraffin-based fuels: thermochemical performance, mechanical properties and ballistic characterization. 2021.

[13] Gary S Haag. *Alternative geometry hybrid rockets for spacecraft orbit transfer*. University of Surrey (United Kingdom), 2001.

[14] Anwer Hashish, Christian Paravan, and Alberto Verga. Liquefying fuel combustion in a lab-scale vortex flow pancake hybrid rocket engine. In *AIAA Propulsion and Energy 2021 Forum*, page 3519, 2021.

[15] MA Karabeyoglu, D Altman, and Brian J Cantwell. Combustion of liquefying hybrid propellants: Part 1, general theory. *Journal of Propulsion and Power*, 18(3):610–620, 2002.

[16] MA Karabeyoglu, D Altman, and Brian J Cantwell. Combustion of liquefying hybrid propellants: Part 1, general theory. *Journal of Propulsion and Power*, 18(3):610–620, 2002.

[17] MA Karabeyoglu and Brian J Cantwell. Combustion of liquefying hybrid propellants: Part 2, stability of liquid films. *Journal of Propulsion and Power*, 18(3):621–630, 2002.

[18] William H Knuth, Martin J Chiaverini, J Arthur Sauer, and Daniel J Gramer. Solid-fuel regression rate behavior of vortex hybrid rocket engines. *Journal of Propulsion and power*, 18(3):600–609, 2002.

[19] Kenneth K Kuo and Martin J Chiaverini. *Fundamentals of hybrid rocket combustion and propulsion*. American Institute of Aeronautics and Astronautics, 2007.

[20] Gyula Mózes. *Paraffin products*. Elsevier, 1983.

[21] Kohei Ozawa, Koki Kitagawa, Shigeru Aso, and Toru Shimada. Hybrid rocket firing experiments at various axial–tangential oxidizer-flow-rate ratios. *Journal of Propulsion and Power*, 35(1):94–108, 2019.

[22] Giulio Panzeri. Pre-combustion and burning characterization of paraffin-based fuels produced by melt- and spin-casting. Master's thesis, Politecnico di Milano, 2021.

[23] Christian Paravan, Riccardo Bisin, Francesco Lisi, Luciano Galfetti, and Pietro Massimo. Burning behavior investigation of a vortex flow pancake hybrid rocket engine. In *AIAA Propulsion and Energy 2019 Forum*, page 4418, 2019.

[24] Christian Paravan, Luciano Galfetti, and Filippo Maggi. A critical analysis of paraffin-based fuel formulations for hybrid rocket propulsion. In *53rd AIAA/SAE/ASEE Joint Propulsion Conference*, page 4830, 2017.

[25] Christian Paravan, Jakub Glowacki, Stefania Carlotti, Filippo Maggi, and Luciano Galfetti. Vortex combustion in a lab-scale hybrid rocket motor. In *52nd AIAA/SAE/ASEE Joint Propulsion Conference*, page 4562, 2016.

[26] Christopher St. Clair, Daniel Gramer, Eric Rice, and William Knuth. Advanced cryogenic solid hybrid rocket engine developments-concept and test results. In *34th AIAA/ASME/SAE/ASEE Joint Propulsion Conference and Exhibit*, page 3508, 1998.

[27] George P Sutton and Oscar Biblarz. *Rocket propulsion elements*. John Wiley & Sons, 2016.

[28] Federico Giambelli Christian Paravan Valerio Santolini, Riccardo Bisin. An overview of splab activities on vortex combustion in a non-conventional hybrid rocket engine. 2023.

[29] Bala Vignesh and Rajiv Kumar. Effect of multi-location swirl injection on the performance of hybrid rocket motor. *Acta Astronautica*, 176:111–123, 2020.

[30] Julian Visinoni. Burning of liquefying paraffin-based fuels in a vortex flow hybrid rocket engine with non-conventional configuration. 2021.

[31] Stephen Whitmore, Zachary Peterson, and Shannon Eilers. Analytical and experimental comparisons of htpb and abs as hybrid rocket fuels. In *47th AIAA/ASME/SAE/ASEE Joint Propulsion Conference & Exhibit*, page 5909, 2011.

[32] Stephen A Whitmore, Sean D Walker, Daniel P Merkley, and Mansour Sobbi. High regression rate hybrid rocket fuel grains with helical port structures. *Journal of Propulsion and Power*, 31(6):1727–1738, 2015.

[33] James R Wilson and Stephen A Whitmore. Pyrolysis of acrylonitrile-butadiene-styrene (abs) under high heat flux conditions. In *50th AIAA/ASME/SAE/ASEE Joint Propulsion Conference*, page 3752, 2014.

[34] Uwe Wolfmeier, Hans Schmidt, Franz-Leo Heinrichs, Georg Michalczyk, Wolfgang Payer, Wolfram Dietsche, Klaus Boehlke, Gerd Hohner, and Josef Wildgruber. Waxes. *Ullmann's Encyclopedia of Industrial Chemistry*, 2000.

[35] Saburo Yuasa, Noriko Shiraishi, Masafumi Sakamoto, Chinatsu Sezaki, Kousuke Hirata, and Takashi Sakurai. Evaluation method of c* efficiency of swirling-oxidizer-flow-type hybrid rocket engines. *Japan Society of Aeronautical Space Sciences*, 59(687):97–101, 2011.

Ringraziamenti

Ringraziamo il nostro relatore di tesi, il Prof. Christian Paravan per averci dato la possibilità e la conoscenza per portare a termine questa attività di ricerca.
Ringraziamo Valerio Santolini, nostro correlatore per i bei momenti passati insieme e per il rigore e la pazienza dimostrata.
Ringraziamo Alberto Verga per il supporto fornito per tutta la durata delle attività in SPLab.
Ringraziamo l'istituzione che è il Politecnico di Milano per gli alti e bassi degli anni trascorsi, che apprezziamo sia ora ma che siamo sicuri ci porteremo dentro per tutta la nostra carriera futura.
Ringraziamo i nostri famigliari per gli sforzi e la fiducia prestati, i quali ci hanno permesso e di portare avanti e completare questo nostro percorso formativo.
Grazie agli amici, tanti o pochi, di lunga data o meno che siano per i momenti condivisi dietro i banchi e per quelli di ricreazione.
L'ultimo ringraziamento, se è concesso, ce lo facciamo da soli, per la conclusione migliore che questi anni di studio potessero avere.

A voi tutti, GRAZIE Luca e Davide